The Winchcombe meteorite-A regolith breccia from a rubble pile CM chondrite asteroid

M. D. Suttle, L. Daly, R. H. Jones, L. Jenkins, M. van Ginneken, J. T. Mitchell, J. C. Bridges, L. J. Hicks, D. Johnson, G. Rollinson, et al.

The Meteoritical Society

Meteoritics & Planetary Science 1–25 (2022)
doi: 10.1111/maps.13938

The Winchcombe meteorite—A regolith breccia from a rubble pile CM chondrite asteroid

M. D. SUTTLE[1,2]*, L. DALY[3,4,5], R. H. JONES[6], L. JENKINS[3], M. VAN GINNEKEN[7], J. T. MITCHELL[8], J. C. BRIDGES[9], L. J. HICKS[9], D. JOHNSON[10], G. ROLLINSON[11], R. TAYLOR[12], M. J. GENGE[13], C. SCHRÖDER[14], P. TRIMBY[15], H. MANSOUR[15], S. PIAZOLO[16], E. BONSALL[14], T. SALGE[2], R. HEARD[2], R. FINDLAY[1], A. J. KING[2], H. C. BATES[2], M. R. LEE[3], N. R. STEPHEN[8], F. M. WILLCOCKS[8], R. C. GREENWOOD[1], I. A. FRANCHI[1], S. S. RUSSELL[2], C. S. HARRISON[2], P. F. SCHOFIELD[2], N. V. ALMEIDA[2], C. FLOYD[3], P.-E. MARTIN[3], K. H. JOY[6], P. J. WOZNIAKIEWICZ[7], D. HALLATT[7,17], M. J. BURCHELL[7], L. S. ALESBROOK[7], V. SPATHIS[7], L. T. CORNWELL[7], and A. DIGNAM[7]

[1]School of Physical Sciences, The Open University, Walton Hall, Milton Keynes MK7 6AA, UK
[2]Planetary Materials Group, Natural History Museum, Cromwell Road, London SW7 5BD, UK
[3]School of Geographical and Earth Sciences, University of Glasgow, Glasgow G12 8QQ, UK
[4]Australian Centre for Microscopy and Microanalysis, The University of Sydney, Sydney, 2006,New South Wales, Australia
[5]Department of Materials, University of Oxford, Oxford OX1 3AN, UK
[6]Department of Earth and Environmental Sciences, University of Manchester, Manchester M13 9PL, UK
[7]Centre for Astrophysics and Planetary Science, Department of Physics and Astronomy, University of Kent, Canterbury, Kent CT2 7NH, UK
[8]Plymouth Electron Microscopy Centre, University of Plymouth, Plymouth PL4 8AA, UK
[9]Space Research Centre, School of Physics and Astronomy, University of Leicester, Leicester LE1 7RH, UK
[10]School of Aerospace, Transport and Manufacturing, Cranfield University, College Rd, Wharley End, Bedford MK43 0AL, UK
[11]Camborne School of Mines, University of Exeter, Cornwall, Penryn TR10 9FE, UK
[12]Carl Zeiss Microscopy, Cambridge CB23 6DW, UK
[13]Department of Earth Science and Engineering, Imperial College London, Exhibition Road, London SW7 2AZ, UK
[14]Biological and Environmental Sciences, University of Stirling, Stirling FK9 4LA, UK
[15]Oxford Instruments Nanoanalysis, High Wycombe HP12 3SE, UK
[16]School of Earth and Environment, University of Leeds, Leeds LS2 9JT, UK
[17]Université de Lille, CNRS, INRAE, Centrale Lille, UMR 8207 – UMET Unité Materiaux et Transformations, F-59000 Lille, France
*Corresponding author. E-mail: martin.suttle@open.ac.uk

(Received 31 May 2022; revision accepted 16 September 2022)

Abstract–The Winchcombe meteorite is a CM chondrite breccia composed of eight distinct lithological units plus a cataclastic matrix. The degree of aqueous alteration varies between intensely altered CM2.0 and moderately altered CM2.6. Although no lithology dominates, three heavily altered rock types (CM2.1–2.3) represent >70 area%. Tochilinite–cronstedtite intergrowths (TCIs) are common in several lithologies. Their compositions can vary significantly, even within a single lithology, which can prevent a clear assessment of alteration extent if only TCI composition is considered. We suggest that this is due to early alteration under localized geochemical microenvironments creating a diversity of compositions and because later reprocessing was incomplete, leaving a record of the parent body's fluid history. In Winchcombe, the fragments of primary accretionary rock are held within a cataclastic matrix (~15 area%). This material is impact-derived fallback debris. Its grain size and texture suggest that the disruption of the original parent asteroid responded by intergranular fracture at grain sizes <100 μm, while larger phases, such as whole chondrules, splintered apart. Re-accretion formed a poorly lithified body. During atmospheric entry, the Winchcombe meteoroid broke apart with new fractures preferentially cutting through the weaker cataclastic

matrix and separating the breccia into its component clasts. The strength of the cataclastic matrix imparts a control on the survival of CM chondrite meteoroids. Winchcombe's unweathered state and diversity of lithologies make it an ideal sample for exploring the geological history of the CM chondrite group.

INTRODUCTION

The Mighei-like (CM) carbonaceous chondrites are the largest class of hydrated meteorites, representing collisionally derived fragments of water-rich asteroids (Browning et al., 1996; McSween, 1979; Suttle et al., 2021; Tomeoka & Buseck, 1985). The number of parent bodies sampled by the CM chondrites, as well as their (former) size and structure, is currently unknown (Cournede et al., 2015; Lee, Cohen, King, et al., 2019; Vernazza et al., 2016). However, their abundance as meteorites found on the Earth (The Meteoritical Bulletin, 2022) and the Moon's surface (Wasson et al., 1975), combined with the widespread occurrence of CM and CM-like fragments in other meteorites (Bunch et al., 1979; Krzesińska & Fritz, 2014; Patzek et al., 2018, 2020), their dominance among the cosmic dust flux (Cordier & Folco, 2014; Engrand & Maurette, 1998; Kurat et al., 1994; Suttle et al., 2017; Taylor et al., 2012) as well as the abundance of asteroids with close spectral matches to the CM chondrites (C-complex asteroids represent >40% of the asteroid belt by mass; DeMeo & Carry, 2013), imply that this group is a large and important class of early solar system materials.

Most (>95%) CM chondrites are recognized as complex breccias containing multiple types of clast. These often exhibit a range of textures and alteration histories (Bischoff et al., 2006, 2017; King et al., 2019; Marrocchi et al., 2021; Vacher et al., 2018; Verdier-Paoletti et al., 2019). Many of the CM chondrites also display well-defined petrofabrics, characterized by subparallel fracture sets and aligned phyllosilicate minerals that wrap around chondrules, forming a foliated texture. These textures are commonly attributed to impact processing (Hanna et al., 2015; Lindgren et al., 2015; Vacher et al., 2018; Verdier-Paoletti et al., 2019). In addition, several CM chondrites have high abundances of solar wind-derived nuclides. This is evidence that they spent significant time exposed as regolith at the surface of their host asteroid (Jenniskens et al., 2012; Krietsch et al., 2021; Nakamura, 2006; Nakamura et al., 1999). Furthermore, rare occurrences of xenolithic material (Ebert et al., 2019) or material assumed to originate from the parent body's deep interior have been reported (Kerraouch et al., 2019). Dynamical analysis of the asteroid belt suggests that the vast majority of objects are impact fragments resulting from the catastrophic disruption of a small number (<150) of planetesimals (approximately >100 km diameter; Delbo et al., 2017). Indeed, current estimates suggest that all asteroids <10 km in diameter are likely to be rubble pile bodies representing the re-accreted debris left over after their primary parent body was disrupted (Walsh, 2018). This hypothesis is supported by the recent direct imaging of the small C-type asteroids (101955) Bennu and (162173) Ryugu by sample return missions. Both bodies were found to be rubble pile asteroids containing unexpectedly coarse, boulder-rich surfaces (Della Giustina et al., 2019; Grott et al., 2020; Lauretta et al., 2019). Multiple lines of evidence therefore suggest that the CM chondrite parent body, or at least one of the parent bodies represented by this group, suffered the same catastrophic disruption fate, leaving behind numerous smaller re-accreted bodies composed of brecciated boulders.

The heterogenous and highly brecciated nature of the CM chondrites raises specific challenges for analysis. Independent research teams analyzing different chips of the same meteorite may arrive at markedly different conclusions regarding the composition, alteration history, and bulk properties. This is particularly problematic where studies have attempted to order CM meteorites into a relative sequence of alteration extents (e.g., Browning et al., 1996; Rubin et al., 2007; Zolensky et al., 1993), as summarized in table 1 of Howard et al. (2009) and table 7 of Cloutis et al. (2011). In response, studies have argued for a revised classification system that reflects the full range of aqueous alteration extents represented by different lithologies within each CM meteorite (Bischoff et al., 2017; Lentfort et al., 2021). This approach aims to better reflect the complex geological histories of these meteorites. However, it also demands more detailed characterization for each new meteorite through a systematic survey on a large, representative area. Thus, the scale of variability within the CM chondrites combined with the lack of an adequate framework to characterize individual lithologies and to keep track of these data between independent research groups has hindered research. Analysis of the new CM chondrite Winchcombe (King et al., 2022) through a consortium effort provides the opportunity to apply the recommendations of Lentfort et al. (2021) while investigating this meteorite's petrography and alteration history.

Based on the analysis of the instrumentally observed fireball, the initial mass of the Winchcombe meteoroid is estimated at 66 ± 6 kg, equivalent to a sphere of rock approximately 0.38 m in diameter (King et al., 2022). Furthermore, numerical modeling of the fireball trajectory

suggested approximately 500 g of rock survived atmospheric entry, while search efforts recovered 602 g. This was found as a main mass (~320 g), a secondary mass (a single stone of 152 g), and several smaller stones dispersed across the strewn field totaling <100 g (King et al., 2022). The Winchcombe meteorite can therefore be thought of as sampling an individual boulder extracted from the surface of a rubble pile parent body.

In this work, we explore the coarse (micrometer to millimeter) scale petrography of Winchcombe through a comprehensive study on multiple polished sections. We focus on the petrographic variation within the meteorite, identifying and characterizing multiple distinct lithologies, evaluating how these lithologies are related, and discussing what this can tell us about the structure of the parent body and geological history of the CM chondrites.

EVALUATING AQUEOUS ALTERATION EXTENT

There are multiple schemes designed to evaluate the relative degree of aqueous alteration in a given CM chondrite lithology: the Browning scale (Browning et al., 1996), the Rubin scale (Rubin, 2015; Rubin et al., 2007), the Howard scale (Howard et al., 2009), and bulk light element analysis (Alexander et al., 2013), as summarized in Suttle et al. (2021). Here, we use the scheme defined by Rubin et al. (2007) because it was designed for the analysis of polished sections under scanning electron microscope (SEM) and because it continues to be widely used by the community.

The Rubin scale varies between an unaltered CM3.0 (an accretionary assemblage, e.g., Kimura et al., 2020) and a completely altered CM2.0 (equivalent to the CM1 designation used elsewhere, e.g., Zolensky et al., 1997). It uses a range of textural, chemical, and mineralogical criteria including matrix composition, Fe-Ni-metal abundance, the percentage of surviving mafic chondrule silicates, the diversity of carbonate and Fe-sulfide minerals, and the chemical composition of a matrix-hosted phase termed tochilinite–cronstedtite intergrowths (TCIs; Rubin et al., 2007).

TCIS IN CM CHONDRITES

One feature that is investigated in detail in this work is the TCI phases. They are an intermixed assemblage of hydrated Fe-sulfide (tochilinite: $Fe^{2+}_{5\text{-}6}[Mg,Fe^{2+}]_5S_6[OH]_{10}$) and Fe-rich serpentine (cronstedtite: $Fe^{2+}_2Fe^{3+}[Si,Fe^{3+}O_5][OH]_4$; Pignatelli et al., 2017; Tomeoka & Buseck, 1985; Vacher et al., 2019). TCIs have been the focus of many previous publications both because they are a unique phase found only in the CM chondrites (e.g., Fuchs et al., 1973; Vacher et al., 2019) and because they are considered to be sensitive indicators of the alteration environment (Lentfort et al., 2021; Pignatelli et al., 2017; Rubin et al., 2007; Tomeoka & Buseck, 1985). TCIs formed relatively early in the aqueous alteration sequence at low temperatures (10–160 °C), under alkaline, reducing, and S-bearing environments (Peng & Jing, 2014; Pignatelli et al., 2017; Vacher et al., 2019; Zolensky, 1984; Zolensky et al., 1993). Later, their compositions evolved as alteration advanced and, consequently, some alteration scales use the compositions of TCIs (e.g., FeO/SiO_2 and/or S/SiO_2) to infer alteration extent (Lentfort et al., 2021; Rubin et al., 2007).

Two types of TCI are recognized based on which precursor phase they replaced (Nakamura & Nakamuta, 1996; Tomeoka & Buseck, 1985). Type I TCIs formed by pseudomorphic replacement of kamacite. They have compact structures and may retain small quantities of residual metal. They are primarily composed of tochilinite but may contain minor quantities of cronstedtite and goethite (Palmer & Lauretta, 2011; Pignatelli et al., 2017). Type I TCIs often reflect the morphology of their precursor metal bead and typically have rounded or irregular shapes (Pignatelli et al., 2017). Type I TCIs occur at low abundances and are often found within altered chondrule cores (Tomeoka & Buseck, 1985). By contrast, type II TCIs have complex zone structures and are proposed to have formed by pseudomorphic replacement, with multiple precursor phases proposed, including anhydrous silicates (olivine and pyroxene; Pignatelli et al., 2016), carbonates (Lee et al., 2014; Vacher et al., 2017), melilite (Lee & Greenwood, 1994), and troilite (Degawa et al., 1995). They may also form by direct precipitation into void space (Tomeoka & Buseck, 1985). Type II TCIs are primarily composed of serpentine, with lesser quantities of tochilinite and occasionally magnetite (Pignatelli et al., 2017; Vacher et al., 2019). They have a distinctive structure with an Fe-rich outer margin and an Mg-rich core. Textures are typically fibrous and acicular, containing many fine-scale filaments with radiating morphologies. In this study, we investigate the formation, alteration, and precursor phases of TCIs.

Note, in this paper, we classify Fe-rich, S-bearing, and Si-bearing alteration phases as TCIs; this follows the conventional treatment in previous publications (e.g., Rubin, 2015; Rubin et al., 2007). However, the relative abundance of tochilinite and serpentine-type minerals within TCIs at submicron transmission electron microscropy (TEM) scales of observation is considered in more detail in a companion paper (Daly et al., 2022).

METHODS

Petrographic Analysis Under SEM

In total, 16 polished sections were generated for this study (Figs. S1–S16); they represent a combined surface

Table 1. List of polished sections investigated in this work.

No.	Fall location	Accession number	Section ID	Institution	Surface area (mm^2)	Lithologies present
1	Main mass (driveway)	BM.2022,M1-87	P30423	NHM/OU	40.2	C
2		BM.2022,M3-29	P30424	NHM/OU	7.5	B, Mx
3		BM.2022,M2-42	P30540	Glasgow	5.9	F, G, Mx
4		BM.2022,M2-43	P30541	Manchester	12.2	D, Mx
5		BM.2022,M2-44	P30542	Kent	7.8	B
6		BM.2022,M2-45	P30543	Leicester	10.8	B, Mx
7		BM.2022,M2-46	P30544	NHM/OU	2.5	B, H, Mx
8		BM.2022,M2-47	P30545	Plymouth	18.9	B, Mx
9		BM.2022,M1-103	P30546	NHM	12.2	B, Mx
10		BM.2022,M1-104	P30547	Zeiss	13.9	B, Mx
11		BM.2022,M1-105	P30548	NHM/OU	8.2	E
12	Secondary mass (field stone)	BM.2022,M9-12	P30550	Cranfield	14.6	A
13		BM.2022,M9-13	P30551	Imperial	7.4	A
14		BM.2022,M9-14	P30552	Glasgow	9.8	A
15		BM.2022,M9-15	P30553	Imperial	9.1	A
16		BM.2022,M9-17	P30555	Imperial	9.1	A
				Total	190.1	

The abbreviation "Mx" is used to denote the cataclastic matrix.

area of 190 mm^2 (Tables 1 and S1). These were produced at the Natural History Museum (NHM), London, in the mineral preparation laboratory. Sections were made from the two largest masses of the Winchcombe meteorite: the main mass recovered from the residential driveway, which disintegrated into many smaller pieces and a mass of fine powder upon impact, and a smaller ~150 g mass found in an agricultural field. All five sections generated from the smaller mass sample the same lithology (A), while sections generated from the main mass sample seven different lithologies. Each section received a preliminary analysis under SEM, generating a whole section backscattered electron (BSE) map and corresponding energy-dispersive X-ray spectroscopy (EDX) elemental maps. These were generated by montaging several tens to hundreds of individual fields, each with a size of 252 × 189 pixels (approx. 555 μm × 415 μm = 0.23 mm^2). Maps were collected on a Zeiss EVO LS15 operating at 20 kV, with a beam current of 3 nA and a total acquisition time for each field of 270 s.

Following preliminary elemental mapping, sections were sent to a range of research groups for further analysis (Table 1). Each institution performed petrographic analysis, identifying and characterizing each distinct lithology present in their section. Several different SEM/EDX systems, based at different institutions, were used in this study. They provided chemical data (spot analyses) on mineral phases (anhydrous silicates, sulfides, magnetite, metal, and chromites) and data from mixed phase regions (e.g. fine-grained matrix and TCIs masses). EDX analyses followed standard best practice protocols, with accelerating voltages of 20 kV and beam currents <3 nA. EDX data were processed using the Oxford Instruments AZtec software. For silicates and oxides, total weight was determined using the "oxygen by stoichiometry" quantification routine, while analyses on metals, sulfides, and carbonate used the "all elements" routine. In addition, electron microprobe analyses (EMPA) were collected on silicate and sulfide phases as well as fine-grained matrix in some sections (P30423, P30424, and P30541). These data were collected at the NHM on a Cameca SX100 EMPA. Analyses used a 20-kV accelerating voltage, a 10-nA beam current, and beam spot of ~1 μm. The Cameca PAP matrix correction software was used to remove artifacts arising from atomic number, absorption, and secondary fluorescence effects. Oxygen was calculated by stoichiometry.

Several lithologies appeared in multiple polished sections while others were represented by only a single section (Tables 1 and S1). We assign labels to each lithology in the form of letter designations (A–H). Lithologies were ordered by apparent abundance (i.e., lithology A is the most abundant and lithology H the least abundant; Table 2). Comprehensive petrographic descriptions for each lithology are given in the supporting information.

Chondrules were identified manually by analysis of BSE images and supporting EDX maps. Outlines were traced by hand and their apparent diameters measured using the ImageJ software (Schindelin et al., 2012) to extract Feret diameters (maximum and minimum lengths), long-axis orientations, and area measurements for each object. The identification of chondrules and former chondrules (pseudomorphs) in aqueously altered meteorites is challenging because secondary mineralization alters the

Table 2. Summary of the eight lithologies identified in this work alongside their properties and alteration extent.

	Exposed surface area			Matrix composition				TCIs				Carbonate		
Lithology	mm^2	%	Chondrule mesostasis	Mg#	S/SiO_2	Metal (area%)	Percent mafic silicate altered	Abundance (area%)	FeO/SiO_2	S/SiO_2	Sulphide	Form	Abund. (area%)	Alteration extent
A	50.0	26.3	Phyllosilicate	63 ± 4	0.12 ± 0.03	<0.3	15–85	34	2.63 ± 0.63	0.56 ± 0.23	Pn	Calcite (T1, T2, chondr. Pseudo.)	4.4	2.2
B	46.7	24.6	Phyllosilicate	66 ± 7	0.09 ± 0.03	<0.1	85–99	22	1.41 ± 0.28	0.23 ± 0.09	Pn, int	Calcite (T2, chondr. Pseudo.)	3.4	2.1
C	40.2	21.1	Phyllosilicate	63 ± 5	0.11 ± 0.03	<0.3	2–15	10	3.12 ± 0.45	0.28 ± 0.19	Pn	Calcite (T0, T1, small clusters)	5.9	2.2/2.3
D	10.2	5.4	Phyllosilicate	59 ± 6	0.11 ± 0.03	>1.4	2–15	—	1.24 ± 0.31	0.10 ± 0.08	Po, Pn	Calcite (T0, T1)	3.3	2.6
E	8.2	4.3	Phyllosilicate	59 ± 3	0.08 ± 0.03	<0.1	15–85	33	2.57 ± 0.31	0.39 ± 0.19	Po, Pn, int	Calcite (T0, T1)	3.4	2.3
F	3.9	2.1	Phyllosilicate	55 ± 9	0.11 ± 0.08	<0.1	100	—	1.14 ± 0.1	0.05 ± 0.02	Pn	Calcite (T2), dolomite	6.7	2.0
G	1.3	0.7	Phyllosilicate	65 ± 7	0.08 ± 0.03	<0.1	85–99	—	1.51 ± 0.12	0.09 ± 0.03	Po, Pn	Calcite (T2, chondr. Pseudo.)	4.7	2.1
H	0.4	0.2	Phyllosilicate	56 ± 6	0.15 ± 0.02	<0.3	15–85	26	3.88 ± 2.14	0.71 ± 0.79	Pn	Calcite (T1)	4.2	2.3/2.4
Mx	29.2	15.4												
Total	190.1	100.0												

Pn = Ni-rich pentlandite; int = pentlandite with intermediate Ni compositions; Po = low-Ni pyrrhotite. The abbreviation "Mx" is used to denote the cataclastic matrix. Metal abundance data were determined either by thresholding of EDX map data using image analysis software. Note some values for TCI composition are shown in gray. These represent lithologies where conventional TCI material was absent; compositions of the meshwork/wormy S-bearing serpentine minerals that form much of their fine-grained matrix are given instead.

composition of chondrules and erodes the boundaries between chondrule and matrix. As a result, chondrule identification in CM chondrites can be subjective. We applied the following criteria when identifying chondrules: (1) circular, ellipsoid, or irregular shapes with diameters <1500 μm; (2) the presence of residual anhydrous silicates (typically Mg-rich olivine) or evidence for the pseudomorphic replacement of anhydrous silicates (Hanowski & Brearley, 2001; Velbel et al., 2012, 2015); (3) the presence of a fine-grained rim (FGR) on the edge of the chondrule, defining the object's outline. Additionally, we note that chondrules often appear as halo shapes seen in single element Na and Ni EDX maps, representing the locally high abundance of Ni-bearing sulfides and Na-bearing phyllosilicates within chondrule FGRs. Petrofabric in each lithology was evaluated by the analysis of chondrule long-axis orientations, where sufficient chondrule statistics permitted. Long-axis orientations were plotted on rose diagrams (Figs. S1–S4, S11 and S14) and are shown as histogram plots in Fig. S17.

Two sections (P30541 and P30548) were analyzed using the automated QEMSCAN® 4300 software (quantitative evaluation of minerals by SEM/EDX) at the Camborne School of Mines, University of Exeter, United Kingdom (Goodall & Scales, 2007; Gottlieb et al., 2000). Sample measurement and data processing used the software packages iMeasure (version 4.2SR1) and iDiscover 4.2SR1 and 4.3. We employed standard QEMSCAN® settings (high vacuum, 25 kV, 5 nA, a 1000 X-ray count rate per pixel, a fixed working distance of ~22 mm, and routine beam calibration every 30 min). The entire exposed surface area of each sample was analyzed using the fieldscan measurement mode (Pirrie & Rollinson, 2011) at an X-ray resolution/pixel spacing of 5 μm and a field size of 1000 μm^2. Data collection and processing followed in-house QC/QA procedures. For details of the QEMSCAN method, see Rollinson et al. (2011) and Andersen et al. (2009). In addition, the modal mineralogy for section P30545 was calculated using a separate technique: the pixel-counting method (Stephen et al., 2010; Yugami et al., 1998) which combines individual element maps in Adobe Photoshop. This was conducted at Plymouth Electron Microscopy Centre (University of Plymouth), using a JEOL 7001F FE-SEM with Oxford Instruments X-Max 50 mm^2 EDS and AZtec v.5.1 software. Imaging and X-ray element mapping were carried out at an accelerating voltage of 20 kV with a probe current of 10 nA. The resulting large area map contained 954 individual fields and 40,655,152 data points at 0.96 μm per pixel resolution.

Calcite grains in section P30555 were analyzed using electron backscatter diffraction (EBSD). This sample, therefore, received extended preparation (2 h 40 min vibratory polishing using a colloidal silica suspension and subsequent carbon coating; 5–10 nm thickness). EBSD analysis was carried out using a Hitachi SU70 Schottky field emission gun SEM located at Oxford Instruments, High Wycombe. We employed an Oxford Instruments Symmetry S2/UltimMax 65 EBSD/EDS detector. Data were collected using the Oxford Instruments AZtec v6.0 acquisition software and processed using Oxford Instruments AZtecCrystal v2.3 software. Data were collected under high vacuum using a 20-kV beam and a probe current of 8.1 nA.

Petrographic Analysis Under TEM

The P30543 section was studied at the University of Leicester Advanced Microscopy Facility. Preliminary BSE imaging and EDX chemical composition measurements were performed using an FEI Quanta 650 field emission gun (FEG)-SEM fitted with an Oxford Instruments AZtec EDX system. This was used to identify the regions of interest for focused ion beam (FIB)-TEM analysis. FIB lift-out sections measuring up to 15 × 8 μm were extracted using an FEI Quanta 200 3D FIB-SEM, thinned to ~100 nm, and attached to 3 mm TEM Cu-grids for TEM analysis. High-resolution TEM imaging and STEM EDX were performed using a JEOL 2100 TEM using the Gatan Micrograph and Oxford Instruments AZtec software packages.

3-D Analysis Using μCT

X-ray absorption contrast tomography data were collected on section P30547 using a ZEISS Context μCT system located at the ZEISS X-ray Quality Excellence Centre in Rugby, United Kingdom. Data were collected at a power of 7 W and 140 kV using a high-energy filter. In total, 2401 projections were collected at an approximate spatial resolution of 5 μm, over the course of ~60-min analysis. The deep learning image enhancement algorithms of DeepRecon Pro (part of the ZEISS Advanced Reconstruction Toolbox) were used to dramatically improve signal-to-noise ratio. We then used the ZEISS Mineralogic 3D automated mineralogy software package to subdivide the data set into regions with statistically different X-ray attenuation values. These divisions were checked against surface observations (BSE and EDX maps) to validate the accuracy of the statistical approach. They allow an approximate determination of morphology and volume proportions for the main features in the P30547 section.

RESULTS

The Winchcombe meteorite is a breccia. The analysis of the 16 Winchcombe sections revealed the presence of

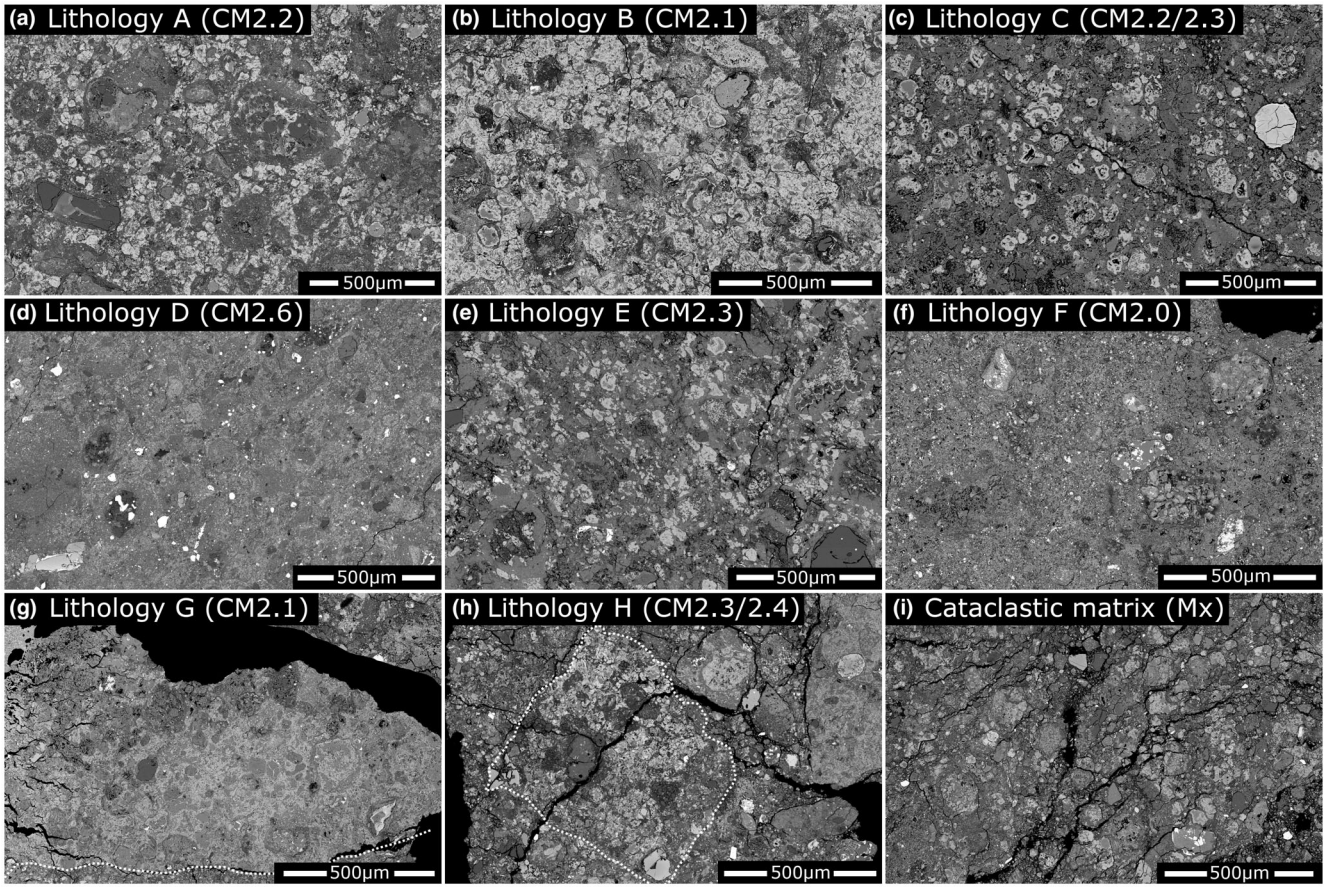

Fig. 1. a–h) Example textures for the eight lithologies identified in Winchcombe. Lithologies range from CM2.6 to CM2.0 although three rock types (A, B, and C) represent >70% of the studied material. Within lithological clasts, the matrix is dominated either by rounded coarse-grained objects (TCIs) as seen in (a–c), (e), and (h) or a finer grained mass of Fe-rich and S-bearing serpentines with a wormy or meshwork appearance as in (d), (f), and (g). i) Texture of the cataclastic matrix (Mx) that holds the breccia clasts together (images are from: a—section P30552, b—section P30542, c—section P30423, d—section P30541, e—section P30548, f—section P30540, g—section P30540, h—section P30544, and i—section P30547).

eight distinct lithologies (Fig. 1). Detailed petrographic definitions for each lithology are given in the supporting information (and summarized in Table 2). There is no evidence for xenolithic material; instead, the various rock types are all CM chondrite lithologies. They represent a range of alteration extents and have variable matrix textures (Fig. 1). This includes rock types recording advanced stages of aqueous alteration (CM2.0–2.3) as well as mildly altered materials (CM2.6). The eight lithologies constitute ~85% of the studied surface area of the Winchcombe meteorite (Tables S1 and 2). The remaining ~15% comprises a heterogenous mix of materials with no coherent alteration extent (Fig. 1I). This includes highly altered TCI material (Figs. 2–4) in direct contact with minimally altered phases such as low-Ni pyrrhotite grains and Fe-rich olivine. This material has a relatively coarse appearance under SEM (with grain sizes typically between 50 and 100 μm) and contains abundant open (unmineralized) fractures and fractured mineral grains. This material exists in between and holds together the lithological clasts and is, therefore, referred to hereafter as the cataclastic matrix (Metzler et al., 1992).

Lithological Units

The three most abundant lithologies (by studied surface area) are A (26.3 area%), B (24.6 area%), and C (21.1 area%). Collectively, they represent 72.0 area% (Table 2). The remaining five lithologies (representing 12.6 area%) are only found as isolated areas within single sections (lithology D in P30541, lithology E in P30548, lithologies F and G in P30540, and lithology H in P30544; Tables 1, 2 and S1). Short petrographic descriptions of each lithology are given below.

Lithology A (Fig. 1a) is highly altered and assigned a CM2.2 petrologic subtype. Chondrules occur at an abundance of 17.8 area% and have a mean average apparent diameter of 110 μm (±60 [1σ], $N = 182$). Most

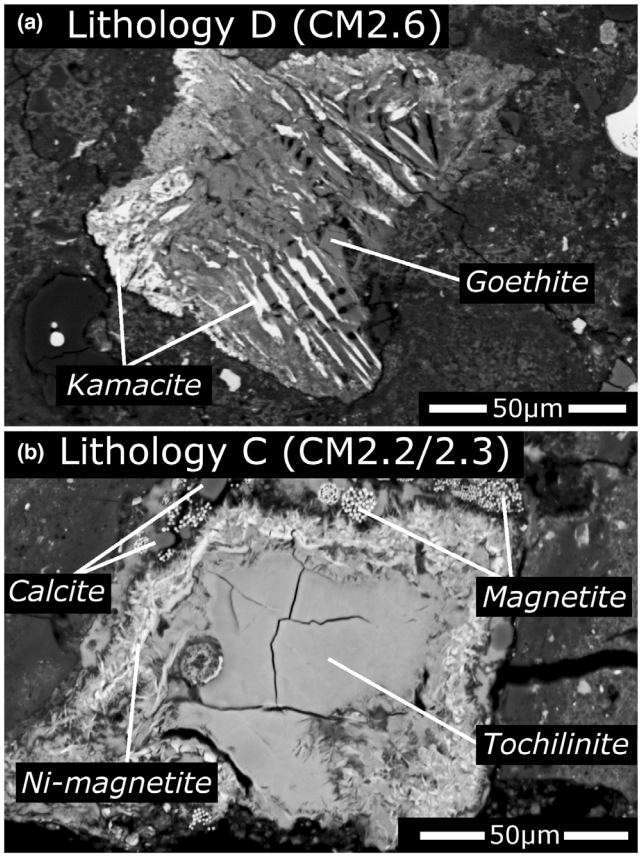

Fig. 2. Diversity of type I TCIs identified in Winchcombe. a) In the least-altered lithology D (found in section P30541), metal is partially replaced by goethite. The example shown here is the most altered metal grain and was selected to highlight the goethite–metal textural relationship. b) More advanced alteration in lithology C (found in section P30423) has completely replaced kamacite grains with tochilinite. Thin margins of Ni-rich magnetite border the grain. A later stage of alteration precipitated magnetite framboids and small calcite grains.

chondrules are ellipsoid although long axes do not appear to be aligned. They have well-defined FGRs with a dark appearance in BSE. Alteration of chondrules is variable, typically with 40–80% of the initial anhydrous silicate content having been replaced (Fig. 5). Pseudomorphic chondrules are rare. The matrix contains abundant type II TCI clusters (34 area%; Figs. 3c and 4). They are composed of multiple smaller individual TCI objects. Each TCI object has sharp boundaries and well-preserved internal textures composed of inward-radiating filaments with multiple nucleation sites. Sulfur-bearing serpentines are also found within the fine-grained matrix. Anhydrous sulfides are exclusively Ni-rich (Ni: 20–34 wt%) pentlandite while carbonates are overwhelmingly T1a calcites (calcite mantled by a rim of tochilinite/serpentine; Vacher et al., 2017), although T2 calcites (calcite grain clusters containing Fe-sulfide or phyllosilicate inclusions; Vacher et al., 2017) and carbonate chondrules are also found. Rare grains of barringerite ($[Fe,Ni]_2P$) are found in lithology A. Magnetite was not identified.

Lithology B (Fig. 1b) is heavily altered and assigned a CM2.1 petrologic subtype. Chondrules occur at low abundance of ~7.0 area% and have an apparent average diameter of 100 μm (±10 [1σ], N = 220). Those that can be identified are extensively altered, with most being near-complete pseudomorphs (Fig. 5). Anhydrous silicates survive in approximately 20% of chondrules where only high-Mg olivine (Mg# > 97) remains. The matrix has a bright (Fe-rich) appearance characterized by abundant coarse-grained type II TCI clusters (Fig. 3b and 3f). They occur at abundances of ~22 area% and have fibrous textures with dark Mg-rich, S-poor cores. Nickel-rich (Ni > 25 wt%) pentlandite also occurs as euhedral rounded or lath-shaped grains. Carbonates are primarily calcite, with T2 varieties being dominant. Dolomitic carbonate was also identified in P30543. Pseudomorphic chondrules replaced by calcite occur occasionally; they contain inclusions of Fe–sulfide and anhedral high-Mg olivine (Fo 99). Rare mixed metal–Fe–sulfide assemblages are found in the matrix (of section P30545); otherwise, metal is preserved only as small droplets held within Mg-rich olivine. Magnetite was not observed.

Lithology C (Fig. 1a) is assigned a CM2.2/2.3 petrologic subtype in the Rubin scale. Chondrules constitute ~10 area%, mean average apparent diameters are calculated at 145 μm (±85 [1σ], N = 231). Chondrule long axes are aligned, and most have clearly resolvable FGRs with a homogenous, compact texture and relatively uniform thickness (30–100 μm). Chondrules show moderate to advanced alteration, although Mg-rich olivine (Mg# > 90) survives with minimal evidence of chemical attack. Altered cores are typically a mix of fibrous Mg-rich phyllosilicates, pentlandite nodules, and magnetite framboids (Fig. 5). The matrix contains small type II TCI clusters, the individual TCI masses that make up the clusters have sharp compositional boundaries and hollow cores. (These are not a product of plucking during polishing because the same features are observed in the μCT data from unpolished regions.) Rare large, rounded type I TCIs are also found (Fig. 2b). Carbonates are exclusively calcite but include multiple generations (Table S2). Small, rounded grains with rims of TCI material (interpreted as T1a calcites; Vacher et al., 2017) are the dominant carbonates, although occasional anhedral masses lacking rims or embedded sulfides (interpreted as T0 calcites; Vacher et al., 2017) are also found. Third-generation carbonates are found in lithology C. They occur as dense clusters of small (1–20 μm-sized) grains with ellipsoidal shapes—these

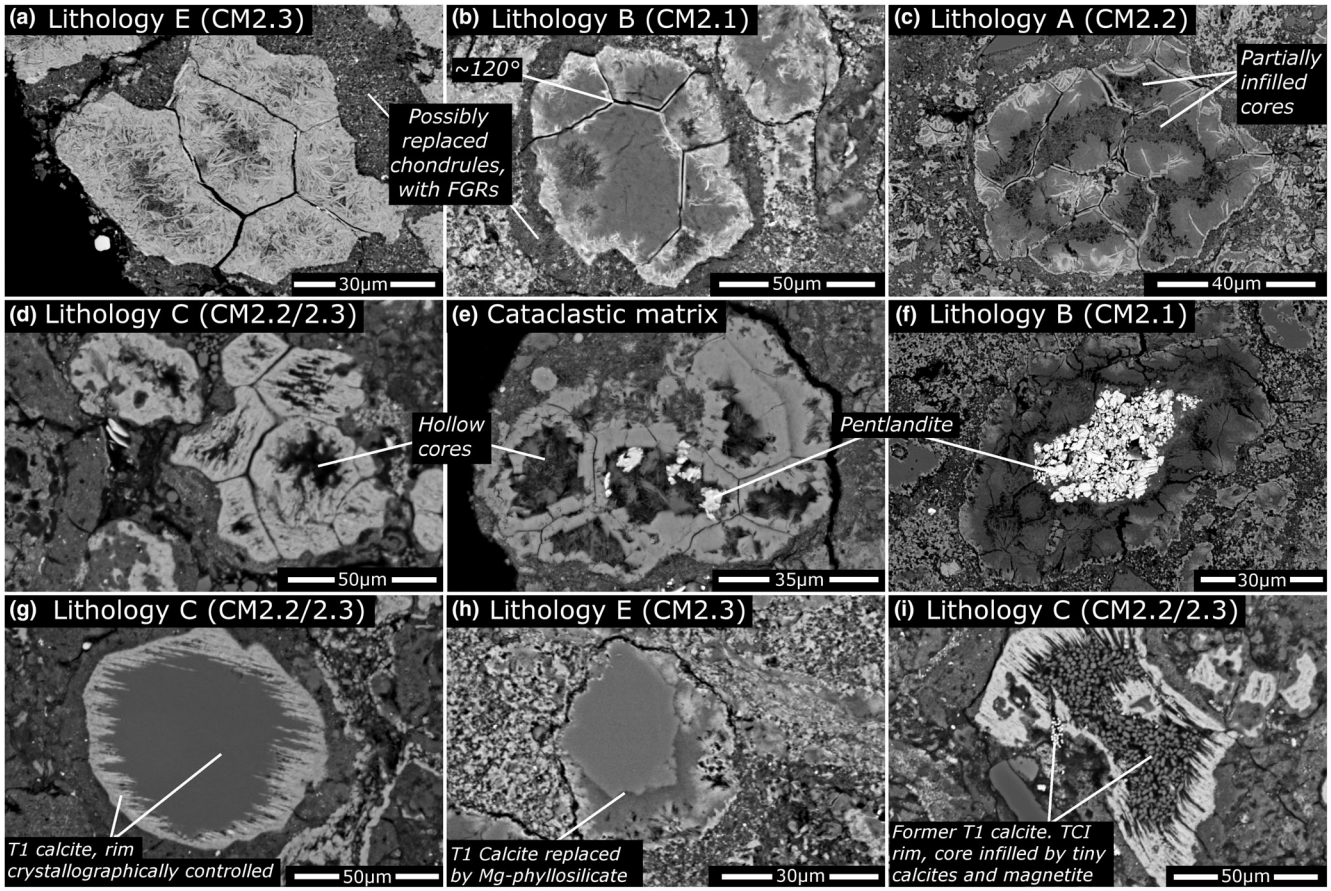

Fig. 3. The diversity of type II (zoned) TCIs. a–f) Type II TCIs are formed by the replacement of anhydrous silicates. a–c) Clusters of TCIs are abundant in several Winchcombe lithologies and often surrounded by dark fine-grained matrix, appearing indistinguishable from chondrule FGRs. Individual TCI masses have a zoned appearance with a bright (Fe-rich) rims and dark (Mg-rich) cores. They are separated from their neighbors by thin open fractures, which may meet at 120° triple points. TCI cores may be infilled (a, b), partially filled (c, f), or hollow (d, e). e, f) Some TCI masses have Fe-sulfide (pentlandite) inclusions in their cores. g–i) Type II TCIs can also form by the replacement of calcite. g) Initially, T1 calcite grains by growth of TCI rims on a carbonate host grain. Later complete dissolution of the calcite host leaves a hollow void that becomes infilled by new secondary minerals, either phyllosilicates (h) or a later generation of carbonate, here with associated magnetite (i) (images are from: a—section P30548, b—section P30542, c—section P30553, d—section P30423, e—section P30544, f—section P30544, g—section P30423, h—section P30548, and i—section P30423).

show a close association with magnetite (Fig. 3i). They are found infilling void space (cracks, fractures, and vugs). These tiny carbonate aggregates do not appear to have been previously described in a CM chondrite. Metal occurs at low abundances in lithology C, although magnetite is common and forms framboid and platelet morphologies.

Lithology D (Fig. 1d) is the least-altered rock type identified and is assigned a CM2.6 petrologic subtype. Chondrules are relatively rare and have a mean average apparent diameter of 170 μm (±70 [1σ], $N = 22$). Based on chondrule long-axis alignment, no petrofabric is discernible (Fig. S17). Both type I and type II chondrule varieties are identified. Olivine is generally unaltered while pyroxene has experienced significant replacement (Fig. 5). Chondrule mesostasis is completely altered to phyllosilicate. TCI structures were not identified in lithology D. Minor alteration of metal (which typically alters to type I TCI material) has formed Ni-poor (Ni < 1.5 wt%) goethite (with low S contents [<1.7 wt%]). Similarly, type II TCIs are absent; instead, much of the fine-grained matrix contains Fe-rich S-bearing (S: 1.1–8.5 wt%) serpentines. These have thin sinuous morphologies that form a wormy or meshwork texture. Individual serpentine phases typically occur as coiled clot-like masses or form overgrowth margins on other phases held within the matrix (e.g., Mg-rich phyllosilicates, carbonates, and sulfide grains). Anhydrous sulfides include low-Ni pyrrhotite with atomic Fe/S ratios of 0.9 (±0.01 [1σ], $N = 31$) as well as Ni-rich (Ni: 28.6 wt%) pentlandite. Carbonates are exclusively calcite—two generations occurring at

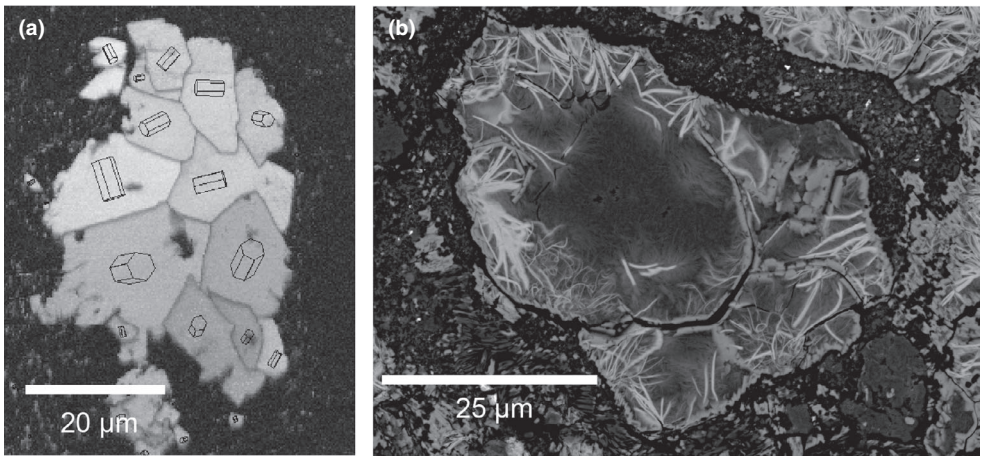

Fig. 4. SEM images of carbonate and TCI textures. a) An electron backscatter diffraction band contrast map of an unaltered calcite grain in lithology A with the unit cell of calcite overlaid onto each grain. The calcite showing straight crystal facets that are parallel to the unit cell and grain boundaries meet at 120-degree triple junctions. b) A BSE image of a TCI formed from the complete replacement of calcite, showing a near-identical texture to the calcite where Fe-rich phyllosilicates decorate and exploited the pre-existing microstructure of the calcite.

approximately equal abundances can be identified. Grain aggregates with irregular shapes, homogenous cores, and an absence of sulfide inclusions or TCI rims are identified as first-generation T0 carbonates (Vacher et al., 2017). In addition, T1a calcites are common. Metal is abundant: Our QEMSCAN analysis measured a value of 0.7 area%. However, this is an underestimate because it does not include small grains (<5 μm) or those affected by beam overlap. We estimate the true abundance to be 1.4–1.6 area% (Table 2). Metal is mostly kamacite with variable Cr contents (<1.0 wt%) although taenite is found as inclusions within a single low-Ni pyrrhotite grain.

Lithology E (Fig. 1e) is assigned a CM2.3 petrologic subtype in the Rubin scale. Chondrules constitute approximately 19.2 area% in lithology E and have a calculated apparent average diameter of 110 μm (±50 [1σ], N = 202). Chondrule shapes are elongated in 2-D section view, and their long axes are aligned, defining a pervasive petrofabric (Figs. S11 and S17). This is one of several defining features that distinguish lithology E from lithology C. Additional differences include different average TCI compositions and TCI abundances and the extent of replaced anhydrous silicates (Table 2). The petrofabric in lithology E is visible not just from elongated chondrules but also from deformed (squashed) TCIs (Fig. 1e). Chondrule silicates have experienced a moderate degree of replacement with 50%–80% of their initial anhydrous silicate budget remaining (Fig. 5). TCIs occur at high abundance (33 area%) and are generally well-preserved type II varieties (Fig. 3a). They have Fe-rich and S-rich compositions. Most TCIs have a homogenous appearance (no zonation) although type II varieties with dark cores are found. Anhydrous sulfides vary in Ni content between intermediate (5 < Ni < 25 wt%) and high-Ni (Ni > 25 wt%) compositions. Carbonates are calcite and include both T0 and T1a generations in approximately equal abundance. A single platinum group metal nugget (~1 μm in size) was found within an Ni-rich pentlandite. Spot EDX analyses qualitatively identified Os, Ir, and Pt.

Lithology F (Fig. 1f) is the most altered rock type found in Winchcombe, assigned a CM2.0 petrologic subtype. Chondrule silicates have been completely altered to phyllosilicate, sulfide, and carbonate (Fig. 5). Despite replacement, secondary phases preserve both former chondrule outlines as well as the internal texture, revealing an abundance of porphyritic chondrules. The reconstructed chondrule abundance is 17.3 area% and their apparent mean average diameter is 140 μm (± 60 μm [1σ], N = 42). As in lithology D, the matrix has a meshwork or wormy appearance owing to the high abundance of Fe-rich (S-bearing) serpentine minerals with vein-like morphologies. Small (<50 μm) rounded Mg-rich phyllosilicate clumps, Ni-rich (Ni > 20 wt%) pentlandites, and carbonates are also embedded within the matrix. Carbonates include calcite and dolomite. Large well-developed T2 calcite are the dominant form. Sulfide inclusions in these phases are tochilinite nodules. Carbonate is also found in chondrule pseudomorphs where it is intermixed with phyllosilicate. Dolomite grains occur either singularly or as mixed phase calcite–dolomite grains. Here, textures reveal dolomite replacing calcite. Kamacite does not survive in lithology F although small chromite and P-bearing metal (Barringerite) grains are present. Magnetite occurs as a trace mineral found within the matrix; qualitatively magnetite is less abundant than in lithology C.

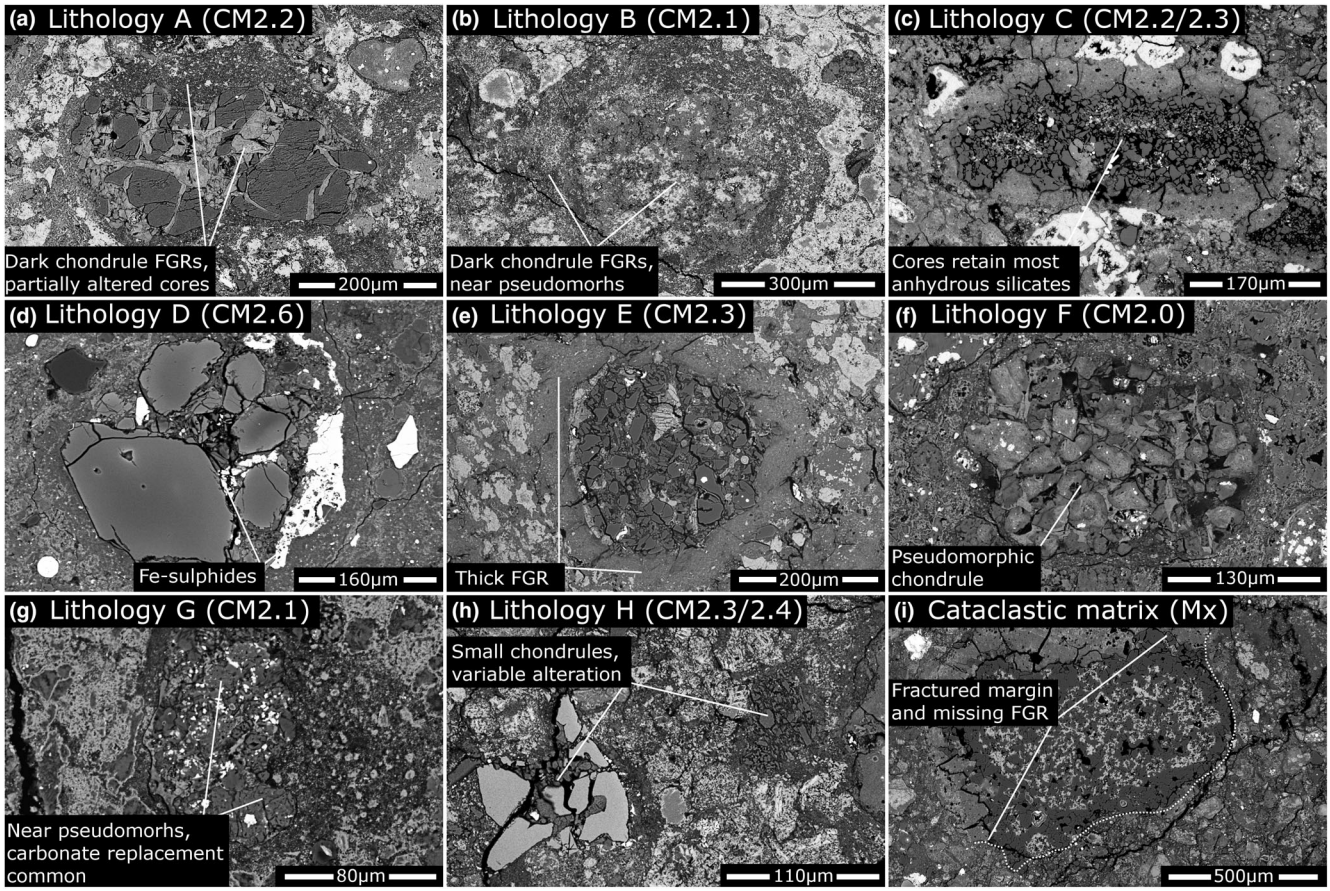

Fig. 5. Chondrule alteration in Winchcombe. Examples of chondrules in each of the eight lithologies (a–h) and (i) a rare whole chondrule (although missing part of the FGR) found within the cataclastic matrix. Chondrule alteration is one of the metrics used to inferred the alteration extent of CM chondrite lithologies (images are from: a—section P30552, b—section P30545, c—section P30423, d—section P30541, e—section P30548, f—section P30540, g—section P30540, h—section P30544, and i—section P30543).

Lithology G (Fig. 1g) is heavily altered and assigned a CM2.1 petrologic subtype. Only a small portion of lithology G is exposed (1.3 mm^2). Only 10 small chondrules were identified; they range in size from 60 to 170 μm. Chondrules are largely replaced by Fe-rich phyllosilicate with minor quantities of calcite (Fig. 5). Typically, <20% of their original anhydrous silicate budget remains. Lithology G is distinguished from lithology B by the conspicuous absence of TCI material; instead, as in lithologies D and F, the fine-grained matrix is composed of S-bearing serpentine minerals with a distinctive wormy or meshwork texture. Anhydrous sulfides include Ni-rich pentlandite (Ni: 24–28 wt%) and Ni-rich pyrrhotite (Ni > 15 wt%). Carbonates are primarily T2 calcite with some calcitic chondrule pseudomorphs. Neither metal nor magnetite was identified.

Lithology H (Fig. 1h) is the least-abundant lithology identified in Winchcombe (0.2 mm^2). Its small size and the variable petrographic properties, which appear to span a range of alteration extents, make assigning an alteration extent difficult. We have tentatively classified lithology H as a CM2.3/2.4. The few chondrules present have diameters <125 μm, modest FGRs, and display a range of alteration states. Most are partially altered type I porphyritic olivine varieties. Between 30% and 80% of the initial anhydrous chondrule silicates have been replaced. The matrix is overwhelmingly dominated by bright, fibrous type II TCI clusters with fine-scale laminated structures. This gives the lithology distinctive texture (Fig. 1h), unlike any of those previously described. By contrast, chondrules are rare, while Ni-rich (Ni: 23–31 wt%) pentlandite and T1a calcite grains are also present. Neither metal nor magnetite was detected.

Chemical Compositions of TCI and TCI-Like Phases

Type I TCIs (formed by the alteration of metal) are relatively rare, with good examples identified only in

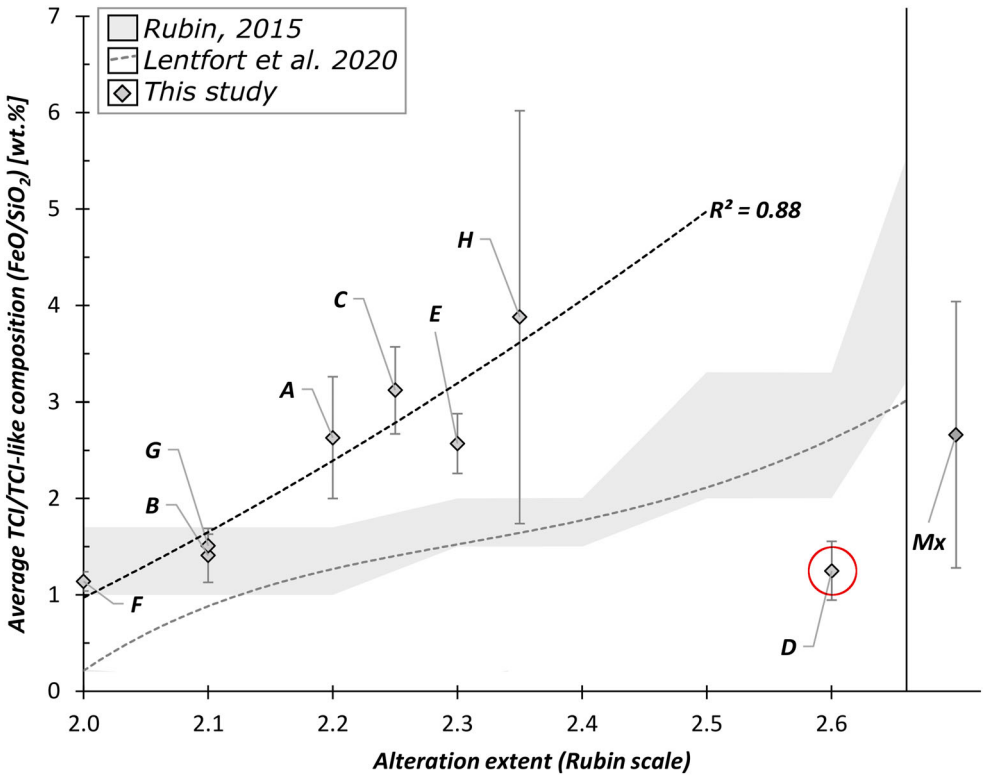

Fig. 6. Average chemical compositions (FeO/SiO_2) of TCI and TCI-like phases in the eight Winchcombe lithologies (and the cataclastic matrix). Error bars mark one standard deviation (1σ). A polynomial trend line is fitted against the data (although lithology D has been omitted from this line of best fit). A high coefficient of determination ($R^2 = 0.88$) demonstrates the close relationship between aqueous alteration extent and TCI compositions. Only lithology D does not fit this trend; its TCI-like phases are instead anomalously Fe-poor. Also shown for reference are the compositional ranges defined in Rubin (2015) and the minimum FeO/SiO_2 values defined by Lentfort et al. (2021) for a given alteration extent. Note, a plot of S/SiO_2 versus alteration extent is given in Fig. S17.

lithologies C and D (Fig. 2). By contrast, type II TCIs (Figs. 3 and 4) are abundant in several lithologies. Well-formed type II structures containing fine-scale laminations of alternating Fe-rich serpentine and tochilinite are found in lithology H. Lithologies A, B, C, and E contain abundant type II TCIs characterized by a zoned appearance with bright Fe- and S-rich rims and dark cores, either hollow (as in lithology C; Fig. 3d and occasionally within the cataclastic matrix; Fig. 3e) or composed of (S-poor) Mg-rich phyllosilicate (Fig. 3a–3f). Some TCI masses have dense Fe-sulfide (pentlandite) inclusions in their cores (Fig. 3e and 3f). In addition, three lithologies (D, F, and G) lack TCI material. Their matrices instead contain thinner vein-like Fe-rich (and S-bearing) serpentine minerals that form wormy or meshwork textures. The average composition of the Fe-rich material in TCIs and TCI-like phases (Table S3) varies between 1.14 and 3.88 wt% for FeO/SiO_2 and between 0.1 and 2.14 wt% for S/SiO_2 (Table 2; Fig. 6). As observed in previous studies, we find a close correlation ($R^2 = 0.88$) between a lithology's average TCI composition and aqueous alteration extent: This relationship is defined by a polynomial trend line:

$$[\text{Average FeO/SiO}_2] = 3.01 \times [\text{alteration extent}]^2 - 5.53 \times [\text{alteration extent}]. \quad (1)$$

We note that our numerical relationship between TCI composition and alteration extent is distinct from the literature values given in Rubin et al. (2007), Rubin (2015), and Lentfort et al. (2021). The reasons for this are explained in the Discussion section.

Figure 7 plots the compositions of core and rim material in zoned type II TCIs, demonstrating that compositions are rarely transitional but are instead bimodal.

Analysis Under TEM

To characterize the main alteration phases, FIB-TEM lift-out sections (Fig. 8) were extracted from section P30543. They sample typical CM chondrite secondary

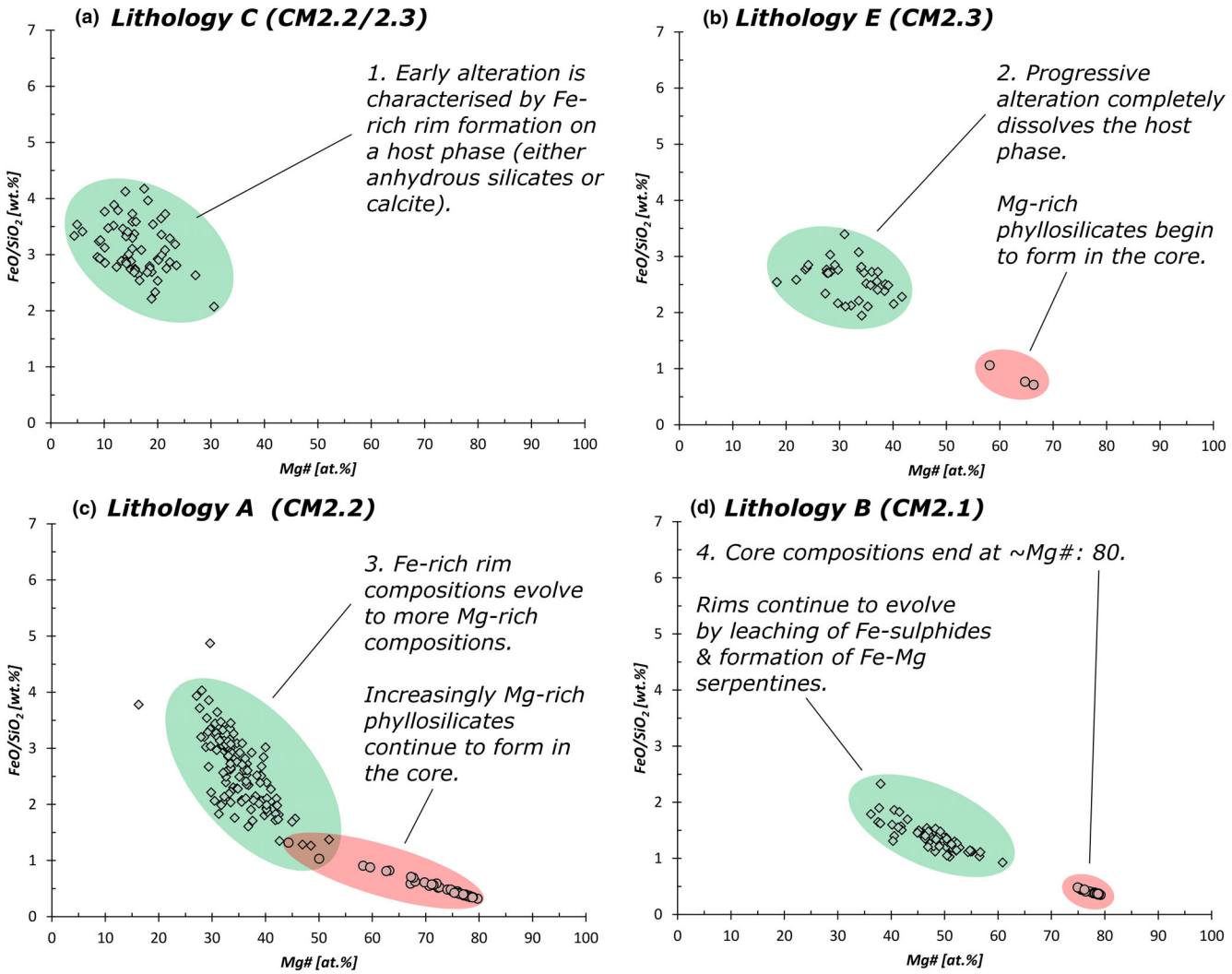

Fig. 7. Compositions of type II TCIs in four of the Winchcombe lithologies (A, B, C, and E). Plots compare the Fe-rich rims (diamonds with green background shading) against the Mg-rich cores (circles and red background shading). These plots illustrate how initial rim formation produces Fe-rich compositions while later core formation occurs under Mg-rich fluids (panels [a] and [b]). The two precipitation windows are separated by a time gap in which fluid compositions evolve and the host anhydrous silicate phase is subject to complete dissolution. After formation, the Fe-rich rim compositions continue to be affected by alteration and evolve toward increasingly Mg-rich compositions (panels [c] and [d]).

phases and were extracted from material within the cataclastic matrix and lithology B. The target area includes tochilinite and S-bearing serpentine, along with small grains (<10 μm) of augite ($En_{35}Fs_{24}$), enstatite ($En_{95}Fs_2$), and pentlandite, all held within a serpentine-rich matrix (Fig. 8a). The majority of the FIB lift-out section consists of tochilinite, as expected from its chemical composition (Table S3). This was further confirmed by observing the predominantly platy crystalline structure in high-resolution TEM analyses. Lattice spacing measurements range from 0.52 to 0.56 nm (Fig. 8c), consistent with tochilinite identified in other CM chondrites (e.g., Mackinnon & Zolensky, 1984; Vacher et al., 2019). The lift-out section also sampled the more abundant serpentine-rich matrix that surrounds the tochilinite. This crystalline serpentine has double-layered lattice spacings measuring ~0.67 to 0.71 nm (Fig. 8d), consistent with serpentine (Hicks et al., 2014). Its chemical composition is given in Table S3. As well as being serpentine-rich, this matrix also featured small particles (<0.5 μm), which are a mix of FeNi-sulfides (likely pentlandite) and a silica polymorph.

Cataclastic Matrix

The cataclastic matrix in Winchcombe (Figs. 1I and 9) is typically observed as small regions adhering to the edge of a lithological clast. In most instances, this

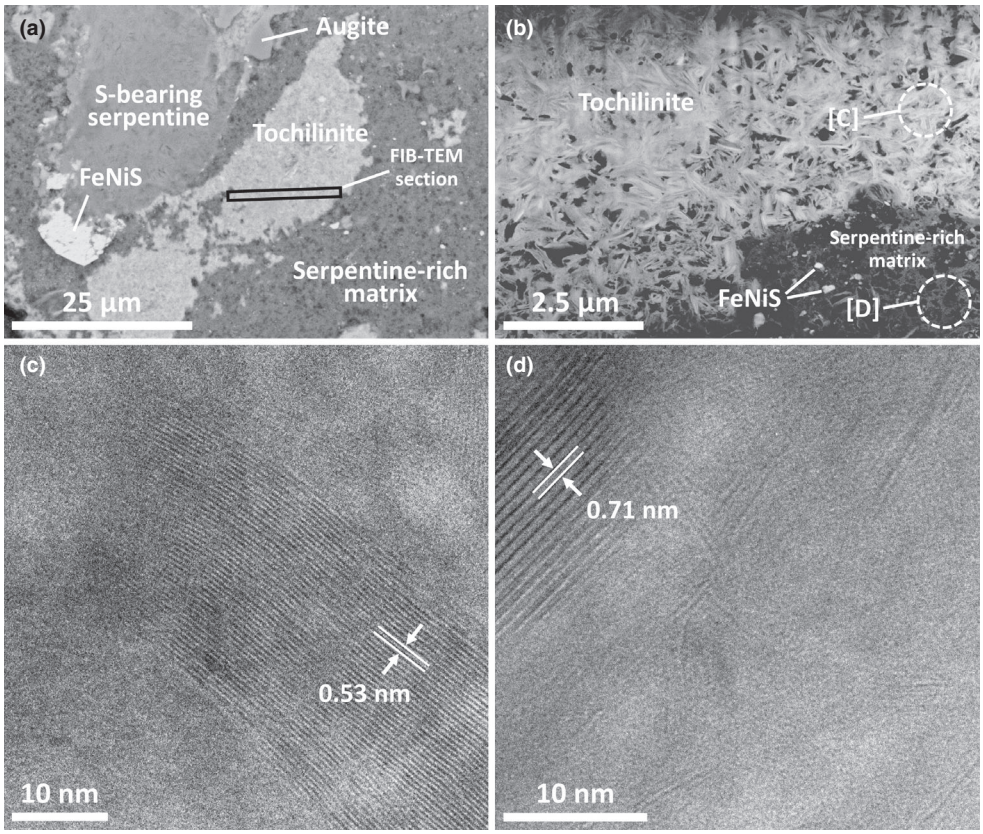

Fig. 8. a) An FIB-TEM lift-out section (location highlighted by the black box) was extracted from a tochilinite mass (from section P30543). b) The lift-out section from (a) approximately measures 11.5 × 7.5 μm, thinned to ~100 nm, containing tochilinite and adjacent serpentine-rich matrix with embedded FeNiS grains. c) Lattice spacings observed in the tochilinite, highlighted in (b), measure 0.53 nm. d) Lattice spacings observed in the serpentine, highlighted in (b), measure 0.71 nm.

material is separated from direct contact with a lithological clast by open fractures, producing sharp unambiguous boundaries. Within the cataclastic matrix, fractures are abundant, pervasive, and often have a dendritic appearance. Regions of cataclastic matrix are found in sections P30424 (1.3 mm^2), P30540 (0.7 mm^2), P30541 (2.0 mm^2), P30543 (7.6 mm^2), P30544 (1.4 mm^2), P30545 (2.3 mm^2), P30546 (0.7 mm^2), and P30547 (13.2 mm^2; Table S1). Together, they represent a combined total of 29.2 mm^2 or 15.4% of the studied surface area (Table 2).

The cataclastic matrix has a coarse, heterogenous texture produced by abundant subangular fragments (typically 50–100 μm) loosely held together within a dark finer grained groundmass (Figs. 1I and 9). Fragments include the full range of CM chondrite components (e.g., Fe-sulfides, whole chondrules with or without FGRs, olivine and pyroxene grains, small silicate fragments, carbonate grains, TCI clusters, as well as coherent blocks of fine-grained matrix with their own distinctive properties; Fig. 9a and 9b). All varieties of Fe-sulfide (low and high Ni pyrrhotites, high and intermediate Ni pentlandites as well as tochilinite grains) are found, although low-Ni pyrrhotites are most common. Likewise, the cataclastic matrix includes the diversity of carbonates (T0, T1a, and T2 calcites, carbonate chondrule pseudomorphs, and dolomite grains). TCI clusters span a wide range of compositions (FeO/SiO_2 ratios range from 1.28 to 4.04 while S/SiO_2 varies from 0.01 to 0.86 [N = 57]) and textures (well-formed to ragged). Both metal and magnetite are also present. The cataclastic matrix is, therefore, a complex mix of components, with both heavily altered and mildly altered phases found in close association. Although a small number of components within the cataclastic matrix are fractured (Fig. 9c–e) with truncated edges, most components are not internally fractured but instead survive as complete grains. Another striking feature of the cataclastic matrix is the apparent low abundance of whole chondrules, <3 area% measured in section P30547 (13.2 mm^2) and <8 area% measured in section P30543 (7.6 mm^2)—these being the two largest regions of cataclastic matrix sampled in this work. However, the small region of cataclastic matrix in P30541 (2.0 mm^2) includes two unusually large intact chondrules (representing 16 area%). They are a 570-μm diameter chondrule composed of largely unaltered forsterite with

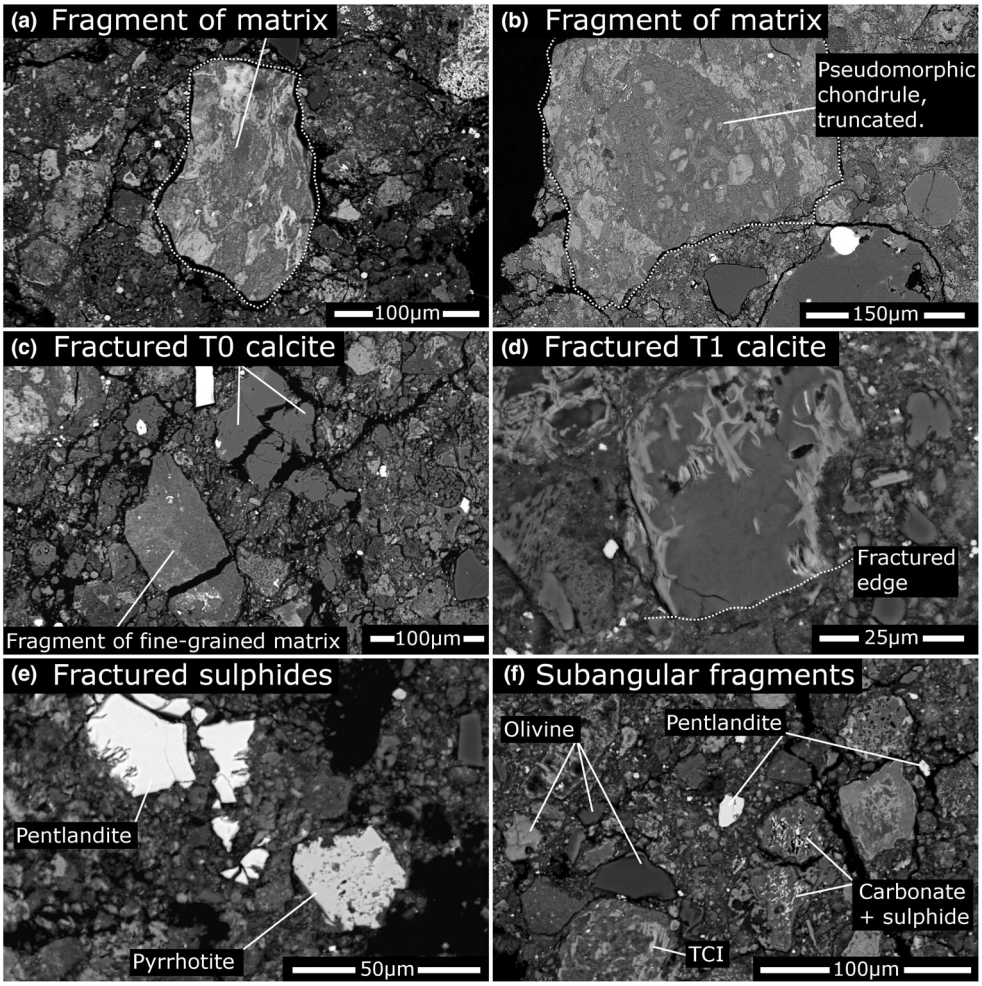

Fig. 9. The cataclastic matrix found in Winchcombe. This material includes (a, b) fragments of fine-grained matrix as well as a diverse mix of mineral grains with variable compositions (c–f). Several (d) grains are themselves fractured (c–e) (images are from: a—section P30547, b—section P30543, c—section P30547, d—section P30544, e—section P30547, and f—section P30424).

metal inclusions, a 150-μm metal grain, diopside, and altered mesostasis; and a 560-μm chondrule with a 100-μm wide FGR, composed of Fe-rich olivine that is partially replaced with fibrous, dark phyllosilicates; minor chromite; and a phosphate grain.

Section P30547 (containing the largest region of exposed cataclastic matrix) was analyzed by μCT, and the resulting 3-D data set interpreted using the automated Mineralogic 3D software. Based on absorption contrast, the data set was separated into three statistically distinct groups (Fig. 10a–c). The lowest Z material corresponds to cataclastic matrix (~82.0 vol%), the intermediate Z material represents lithological clasts (~16.7 vol%), and the highest Z material identifies high-density mineral phases (being a mix of Fe-sulfides, Fe-oxides, and Fe-Ni-metal, ~1.4 vol%). Ignoring the high-density mineral phases (which are in both the cataclastic matrix and the lithological clasts) allows an estimation of the ratio of clasts to cataclastic matrix in section P30547—this is approximately 1:5. In total, 44 clasts were identified in P30547. They range in volume from 2×10^4 to 8×10^6 μm^3. However, two large clasts dominate (occupying 47.1% and 36.5% of the total clast volume, respectively). These are seen in Fig. 10d as the yellow and brown regions. They are separated by a large fracture that cuts through the approximate center of the P30547 section. The remaining clasts are all small (each <2.7% of the clast volume).

DISCUSSION

The Winchcombe meteorite is a breccia composed of clasts of CM chondrite material held together by a fragmented cataclastic matrix. Clasts record the localized geological history of their first-generation parent body, prior to brecciation and re-accretion. Because boundaries

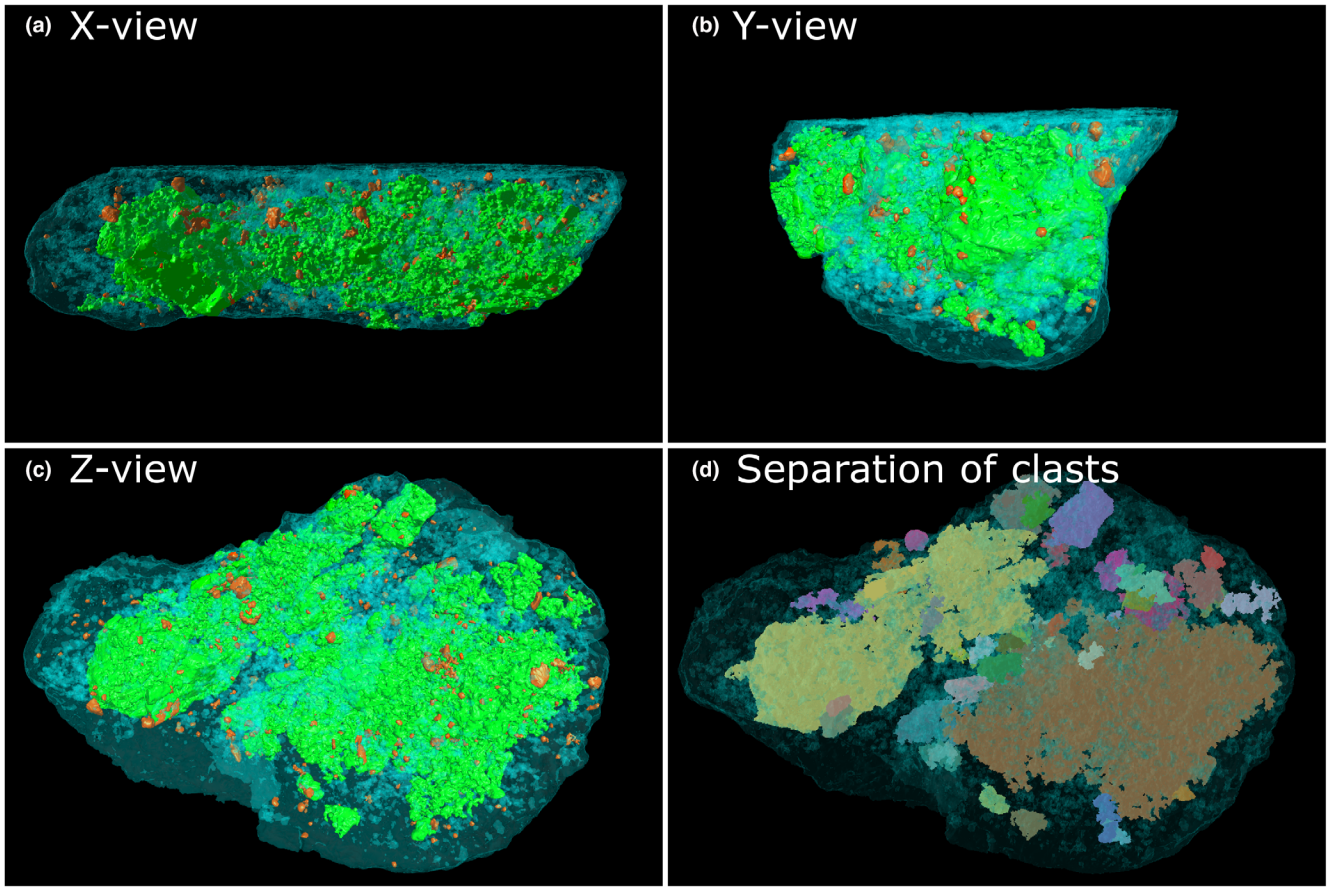

Fig. 10. Micro-CT data collected on section P30547 and subsequent interpretation. a–c) Data were segmented into three divisions: low-Z (blue) corresponds to cataclastic matrix, intermediate-Z (green) corresponds to lithological clasts, and high-Z (red) corresponds to high-density mineral phases. d) Visualization of the clast population (shown in a range of colors). In total, 44 clasts were identified, ranging in volume from 2×10^4 to 9×10^6 μm^3.

between clasts are compositionally sharp (Figs. 1g, 1h, and 10d) and often defined by open fractures, this implies that aqueous alteration did not continue after brecciation (at least not significantly). Outside the fusion crust, none of the lithologies (nor the cataclastic matrix) display evidence of high-temperature alteration. For example, phyllosilicate dehydration cracks and carbonate decomposition products are absent. Winchcombe, therefore, contains no evidence of post-hydration thermal metamorphism.

The range of alteration extents represented in Winchcombe allows investigation of mineral evolution during the aqueous alteration. Here, we focus on the evolution of TCIs. The discussion also considers the formation of the cataclastic matrix and, therefore, the post-hydration history of the CM chondrites.

Alteration of Metal to Form Type I TCIs

During the early stages of CM chondrite alteration, metal was altered to tochilinite (plus minor cronstedtite and goethite) thereby forming type I TCIs (Palmer & Lauretta, 2011; Pignatelli et al., 2017; Tomeoka & Buseck, 1985). In Winchcombe, a range of metal alteration responses is observed.

In the least-altered lithology (D, CM2.6), type I TCI structures (as described in the literature) are absent. Instead, the alteration of metal has resulted in the formation of Ni-poor (Ni < 1.5 wt%) goethite, which presents either as thin rims on metal grains or as rare larger goethite masses containing residual kamacite inclusions (Fig. 2a). The apparent absence of tochilinite and cronstedtite indicates that both S- and Si- activities remained low during metal alteration. Under these conditions, Palmer and Lauretta (2011) concluded that magnetite should form. Instead, the presence of goethite in lithology D implies more oxidizing conditions. Alteration of kamacite to goethite was previously identified in the CM chondrites Murray, Murchison, Allan Hills (ALH) 81002 (Hanowski & Brearley, 2000), and in the recently classified Reckling Peak (RKP) 17085 (Musolino, 2021). In these samples, kamacite was

dissolved, and the Fe redeposited throughout the matrix as veins of goethite with aureole-like structures that surround mineral grains, chondrules, and other chondritic components. Hanowski and Brearley (2000) argued that their radial symmetry was evidence of limited fluid flow and highly local alteration reactions. By contrast, in Lithology D, the alteration of metal to goethite is not associated with vein formation or widespread Fe mobilization. Instead, metal appears to have altered in situ without significant dissolution and transport in the fluid phase.

Recent hydrothermal alteration experiments on the CO chondrite Kainsaz under low temperature, oxidizing, and open system conditions produced similar features to lithology D. Kamacite was altered to goethite without concurrent tochilinite or cronstedtite formation (Suttle et al., 2022). The crystalline matrix of Kainsaz limited the dissolution of sulfides and silicates (keeping dissolved S and Si activities low), while the open system loss of H_2 promoted oxidizing conditions, preferentially forming goethite instead of magnetite. Evidence for H_2 degassing has been identified in both the CR and CM chondrites (Eiler & Kitchen, 2004; Elmaleh et al., 2015; Le Guillou et al., 2015; Pignatelli et al., 2017) and similar conditions likely affected lithology D. By contrast, fluid-limited geochemical microenvironments could have kept S- and Si- activities low around metal grains during their alteration. Microenvironments appear to have been relatively common features in the CM chondrites, especially during the early stages of aqueous alteration (Brearley, 2006; Pignatelli et al., 2016; Suttle et al., 2021; Vacher et al., 2017; Verdier-Paoletti et al., 2019), and may explain the presence of goethite in lithology D.

Lithology C (CM2.2/2.3) is more altered than lithology D (CM2.6). Here, three large grains of tochilinite were identified (Figs. 1c and 2b). They are interpreted as type I TCIs formed by alteration of metal grains. They have rounded or irregular shapes, sized between 20 and 160 μm, and are composed of dense tochilinite cores with rims of Ni-rich (Ni: 21.0 wt%) magnetite (Fig. 2b). Low Si contents (<2.5 wt%) indicate minimal co-precipitation of phyllosilicate. In addition, these phases are surrounded by mixed assemblages of framboidal magnetite and rounded calcite. No residual metal survives. They represent more heavily altered type-I TCIs than those described by Tomeoka and Buseck (1985) or Pignatelli et al. (2017). In lithology C, initial sulfidation of kamacite produced a Ni-poor tochilinite (Ni < 2.5 wt%), with the dissolved Ni being locally reprecipitated as Ni-magnetite. Hydrothermal experiments by Vacher et al. (2019) demonstrated that tochilinite precipitates under reducing, alkaline (pH > 11.5), and S-rich fluids and at low temperatures (<160 °C). This is in contrast to the conditions required to form the later co-precipitated magnetite–carbonate assemblage that surrounds the type I TCIs in lithology C. They formed under S-poor, alkaline, and oxidizing conditions (Jilly-Rehak et al., 2018). The type I TCIs in lithology C therefore attest to evolving fluid conditions, notably transitions toward more oxidizing environments.

The Formation Mechanism for Type II TCIs

Type II TCIs are common alteration phases in several Winchcombe lithologies (A, B, C, and E) and present with a diversity of morphologies (Figs. 3 and 4) and compositions (Figs. 6 and 7). Large TCI clusters, composed of multiple smaller TCI objects, are common in the three most abundant Winchcombe lithologies (A–C). The individual TCI objects that make up these masses have bright Fe-rich rims and dark cores (either hollow or Mg-rich). The Fe-rich outer rims contain variable quantities of Si and S indicating mixed phase phyllosilicate–sulfide compositions. Meanwhile, the cores of TCIs are always S-poor ($S/SiO_2 < 0.3$, S < 4.0 wt%) and Si-rich (~16 wt%) indicating a phyllosilicate-dominated mineralogy. Type II TCI formation occurred by inward replacement (Pignatelli et al., 2016) of a precursor phase (the identity of which is discussed below). The rims formed first, and their compositions suggest that the attacking fluids were initially Fe-rich and S-rich (Pignatelli et al., 2017; Vacher et al., 2019).

In Winchcombe, we observe numerous examples of hollow TCI structures (rims without infilled cores). These are seen in lithology C (Fig. 3d) and within the cataclastic matrix (Fig. 3e). They represent that the TCI formed after rim development and before the core material was deposited. The presence of hollow structures is evidence that, after rim deposition, TCI formation generally progressed by extended dissolution without concurrent secondary mineralization. The infilled cores of TCIs are dark and have a drusy appearance (e.g., Fig. 3b). This implies that the Mg-rich phyllosilicates precipitated into fluid-filled voids left after the precursor phase had completely dissolved. Initially, this generated phyllosilicates with a porous fibrous texture (Fig. 3c); however, these subsequently matured into more compact deposits (Fig. 3b and 3c).

One striking feature of the type II TCI structures is their zoned appearance with a well-defined compositional boundary between the core and rim (Figs. 3b, 3c, 3f and 7). Multiple previous studies have demonstrated that during CM chondrite alteration, the species and cation composition of secondary minerals were controlled by the composition of the fluid phase, and not the host mineral being replaced (Hanowski & Brearley, 2001; Lee et al., 2014; Velbel et al., 2012, 2015). Therefore, the zoned structure attests to an abrupt change in fluid

chemistry from initially Fe-rich and S-rich compositions to Mg-rich, S-poor compositions. Thus, under the conditions of TCI core formation, the outer early formed rims would have been unstable and subject to chemical reprocessing. Evidence for this can be seen by comparing the TCI rim compositions in lithologies with different alteration extents (Fig. 7). In the more heavily altered rock types (e.g., lithology B [CM2.1, Fig. 7]), rim compositions extend to lower FeO/SiO_2 ratios and have more Mg-enriched compositions. The chemical alteration of TCI material is a well-established trend in CM chondrites and one of the principal metrics to infer alteration extent (e.g., Browning et al., 1996; Lentfort et al., 2021; McSween, 1979; Rubin et al., 2007). Rubin et al. (2007) concluded that the loss of TCI masses in the most heavily altered CM chondrites (<CM2.2) is a diagnostic feature of advanced alteration. More recently, Van Kooten et al. (2018) demonstrated that the reaction of dissolved silica with tochilinite can form troilite/pyrrhotite group sulfides and Mg-rich serpentine while also liberating water to drive new alteration reactions:

$$18FeS \cdot 5[(Mg,Fe]OH_2)_{(s)} + 9\ SiO_{2(aq)} \rightleftharpoons 18FeS + 5(Mg,Fe)_3Si_2O_5(OH)_{4\ (s)} + 5H_2O(aq). \quad (2)$$

In general, the bulk S/SiO_2 ratio of TCI phases decreases as alteration advances (Table 2) (Rubin et al., 2007) suggesting that most of the newly formed sulfide was precipitated outside the TCI (within the matrix). This process had the effect of increasing TCI phyllosilicate-to-sulfide ratio. However, examples of local sulfide formation as coarse nuggets of pentlandite deposited in the center of TCI structures are observed (Fig. 3e and 3f). The end stages of TCI alteration were, therefore, characterized by phyllosilicate growth combined with scavenging of sulfur to form concentrated, chemically resistant sulfide deposits.

What Precursor Phases Did Type II TCIs Replace?

Type II TCIs form primarily by the replacement of a precursor phase, typically either anhydrous silicates (Pignatelli et al., 2016) or carbonates (Lee et al., 2013, 2014; Vacher et al., 2017). Direct evidence of these reactions, in which both the precursor and replacing phase are preserved, has been reported (fig. 5 in Vacher et al., 2017; fig. 8 in Lee et al., 2014; and fig. 8 in Pignatelli et al., 2016). In this study, Fig. 3h adds to this list with the observation of anhedral calcite in the core of a zoned type II TCI.

Most previous studies analyzing TCI precursors have focused on the smaller individual TCI objects, which typically have sizes <100 μm. However, CM chondrites also contain larger TCI structures that may have different precursor phases. Larger TCI clusters are abundant in Winchcombe and are composed of multiple smaller objects, each with its own zoned appearance (Fe-rich rim, Mg-rich core). The constituent TCI objects are separated from their neighbors by thin, straight, open fractures that meet at a range of angles, including 120° triple-point junctions (Fig. 3b). These textures bear a striking resemblance to the large carbonate grain clusters also found in Winchcombe (Fig. 4a). They are composed of interlocking, euhedral subgrains with flat, well-defined grain boundaries, and 120° intersections. During parent body alteration, fluids would have attacked these carbonate clusters by penetration along subgrain boundaries. Replacement by Fe- and S-rich fluids produced the characteristic Fe-rich rims whose outlines pseudomorph the former carbonate subgrain boundaries resulting in the observed TCI clusters found in Winchcombe and other CM chondrites.

Limitations of TCI Composition to Infer Alteration Extent

Figure 6 compares the average TCI composition (FeO/SiO_2) of each lithology against their assigned alteration extent (petrologic subtypes). We observed a correlation between FeO/SiO_2 ratio and alteration extent (Fig. 6) and between S/SiO_2 ratio and alteration extent (Fig. S18). However, these relationships are distinct from that defined by previous studies (Lentfort et al., 2021; Rubin, 2015; Rubin et al., 2007). Often, we found that, on the basis of a TCI composition, the various Winchcombe lithologies should be assigned higher (less-altered) petrologic subtypes if the recommendations of Rubin et al. (2007), Rubin (2015), and Lentfort et al. (2021) were followed. However, to do so would have ignored other criteria that pointed to lower (more-altered) petrologic subtypes. For example, the average TCI compositions of lithology A implies a CM2.5 classification; however, a CM2.5 should also have unaltered chondrule silicates and a mix of pyrrhotite and pentlandite within the matrix. In lithology A, we find heavily altered chondrule silicates and only pentlandite, such features are associated with advanced alteration (<CM2.4; Rubin et al., 2007). As a result, although we elected to apply the Rubin scale, we gave each criterion approximately equal weighting. This is in contrast to the recent work of Lentfort et al. (2021), who concluded that accurate subclassification of CM lithologies can be achieved by considering only TCI composition (specifically FeO/SiO_2 ratio). We argue that approximately equal weighting of the Rubin scale criteria is justifiable for several reasons:

1. TCIs are absent in some of the Winchcombe lithologies (D, F, and G), preventing use of the TCI metric.
2. TCI compositional range can vary significantly within a lithology and may even span a range characteristic of multiple different petrologic subtypes (Fig. 6). This means that a single mean average may be unrepresentative, masking the sample's complexity.
3. Given the high degree of variability that can arise, large numbers of analyses are required to accurately evaluate the statistical variation in TCI composition, and this may not be possible for small sample areas.
4. One of the original motivators for the Rubin et al. (2007) scale was the use of several metrics to ensure a more comprehensive assessment of alteration extent.

Large variations in TCI composition could be a result of two factors:

1. During the early stages of aqueous alteration, geochemically isolated microenvironments appear to have been common (Brearley, 2006; Daly et al., 2022; Pignatelli et al., 2016; Suttle et al., 2021; Vacher et al., 2017; Verdier-Paoletti et al., 2019). TCI formation also occurred early in the aqueous alteration sequence (Leroux et al., 2015; Rubin, 2015; Vacher et al., 2017) and potentially under these microenvironment conditions (Pignatelli et al., 2016, 2017; Vacher et al., 2019). Therefore, in the less-altered CM chondrite lithologies (that have not been affected by later fluid reprocessing), variability in TCI compositions may reflect the diversity of different fluid pockets.
2. During the later stages of aqueous alteration, TCI compositions were reprocessed by fluids and their compositions evolved. This is the basis for using TCI composition as an indicator of alteration extent. However, reprocessing was incomplete, as evidenced by the heterogenous composition of TCIs within a single lithology (Fig. 7). This spread therefore records the evolution in fluid compositions over the course of the parent body's aqueous alteration and not the average extent of alteration.

These two factors mean that over-reliance on TCI compositions to infer alteration extent in CM chondrites may lead to erroneous assessments.

The Cataclastic Matrix and Parent Body Brecciation

Most CM chondrites are recognized as breccias (Bischoff et al., 2006, 2017; King et al., 2019; Vacher et al., 2018; Verdier-Paoletti et al., 2019). By definition, breccias contain a cement that holds the component clasts in place although this host material is rarely studied (e.g., Nakamura et al., 1999), with most previous work instead concentrating on the primary accretionary rocks (the lithological clasts).

Brecciation in chondrites may have been a result of (1) impact disruption (Bischoff et al., 2006; Nakamura, 2006; Vacher et al., 2018); (2) or self-disruption, arising due to the explosive release of gases (primarily H_2) generated during aqueous alteration (Alexander et al., 2010; Rosenberg et al., 2001; Wilson et al., 1999). Distinguishing between these scenarios remains difficult and requires independent evidence of shock processing.

In Winchcombe, numerous lithological clasts with variable aqueous alteration extents and abrupt boundaries are found in close juxtaposition. This comminuted texture is consistent with formation by fragmentation and mixing of debris derived from the entire clast population. However, the key evidence in support of impact brecciation is the occurrence of elongated and aligned chondrules (found in some lithologies). These petrofabrics are observed in several CM chondrites and interpreted to form by flattening during impact (Hanna et al., 2015). Therefore, we suggest the most likely origin of brecciation in Winchcombe was impact disruption leading to the excavation of material from different regions within an inhomogeneous CM chondrite asteroid. The excavated material would have re-accreted as a mix of fines and larger fragments (the lithological clasts) forming either a second-generation rubble pile asteroid, or a fallback breccia on the original parent body.

The presence of water (both pore water and hydrated minerals) affects how asteroids respond to hypervelocity impact. Impact experiments (~5 km s^{-1}) into wet sandstone targets demonstrate that pore water reduces the peak pressure experienced at grain boundaries, thereby inhibiting grain comminution (transgranular fracture) while reducing shock wave attenuation, allowing for deeper penetration into the target (Baldwin et al., 2007; Buhl et al., 2013). Experimental studies impacting hydrated CM chondrites have concluded that these meteorites preferentially respond by catastrophic disruption even at relatively low velocities (2 km s^{-1}; Flynn et al., 2009), producing abundant small fragments (<100 μm; Flynn et al., 2005, 2009; Tomeoka et al., 2003). Tomeoka et al. (2003) explored higher peak pressures and demonstrated that phyllosilicate minerals experience thermal decomposition above 30 GPa. In Winchcombe, the absence of dehydrated phyllosilicates and the non-detection of shock melt constrain disruption pressures to below 21 GPa. Meanwhile, the coarse texture and high abundance of whole (unfractured) components (e.g., complete carbonate grains, Fe-sulfides, and TCI clusters) implies that during fragmentation,

fractures preferentially propagated around most phases rather than cutting through them (intergranular fracture). However, an exception appears to be chondrules, which are generally rare in the cataclastic matrix (typically <10 area%). The paucity of whole chondrules might, therefore, be a result of their catastrophic disruption during brecciation. This suggests that intergranular fracture dominates at grain sizes <100 μm while transgranular fracture dominates at coarser scales (>100 μm). The grain size of the Winchcombe cataclastic matrix therefore closely agrees with the debris distributions generated by hypervelocity impact experiments into CM chondrites (Flynn et al., 2005, 2009; Tomeoka et al., 2003).

After re-accretion, some form of lithification must have occurred to give the cataclastic matrix its (low) cohesive strength. The nature of this cement is unknown because we did not identify interpenetrative mineral growth and simple electrostatic effects would be insufficiently binding. Upon impact with the ground, the main mass disrupted into abundant powder with a few larger stones (<9 g; King et al., 2022). These stones were sampled by sections P30423–P30548 and were found to sample a range of lithologies, with adhering cataclastic matrix (Table 1; Figs. S1–S16). Conversely, the secondary mass survived impact with the ground without fragmentation (albeit into soil rather than concrete) and was found to be a single lithology (A). The studied sections also lack adhering cataclastic matrix. Overall, these features imply that the cataclastic matrix is weaker than the embedded lithological clasts and that as the Winchcombe meteoroid fragmented, cracks preferentially cut through the weaker cataclastic matrix thereby liberating lithological clasts. Numerical modeling of the meteoroid indicates that the stone survived dynamic pressures <0.5 MPa during atmospheric entry (McMullan et al., 2022), giving a minimum approximate strength value for the cataclastic matrix. Furthermore, McMullan et al. (2022) argue that for any higher dynamic pressures, Winchcombe would not have survived. This meteorite is, therefore, an example of an unusually weak CM chondrite that would not typically survive atmospheric entry.

The post-depositional evolution of the cataclastic matrix is recorded in the abundance of fractures. Fracture density is variable, with some areas almost fracture-free, and others dominated by linear, or bifurcating, fracture sets. Fractures tend to surround more competent clasts, often bounding them on all sides. Grain sizes in these areas are small. Such textures resemble cataclasites (e.g., fig. 7 in Schröckenfuchs et al., 2015), in which grain size reduction occurs as a result of high strain rates. The textural resemblance to cataclasites implies lateral displacement of clasts and shearing. Such mechanical deformation might occur during the propagation of a shockwave through a polymict breccia, since velocity will be higher through those clasts with the highest sound velocity and lower through the cataclastic matrix. The dense fracture networks observed in Winchcombe further lower the strength of the cataclastic matrix making this material prone to brittle failure and disintegration during atmospheric entry.

IMPLICATIONS AND RELATIONSHIP TO OTHER CM CHONDRITES

To date, the CM chondrite group includes 721 meteorites, of which just 21 are confirmed falls (The Meteoritical Bulletin, 2022). Among these, Winchcombe is both the most recent fall and one of the most rapidly isolated from the terrestrial environment (King et al., 2022). Furthermore, Winchcombe is one of only five carbonaceous chondrites with a well-constrained pre-atmospheric orbit (McMullan et al., 2022). The pristine nature of the sample (minimal terrestrial weathering) combined with its precise outer Main Belt origin makes this meteorite the ideal candidate for investigating the geological history of the CM chondrite group.

Winchcombe is notable for its relatively high abundances of zoned type II TCIs, including large TCI clusters (>150 μm). These are found in all three of the main lithologies (lithologies A–C; Fig. 1). Their analysis provides insights into the chemical environment, the sequence of secondary mineralization, and the evolution of fluid compositions during aqueous alteration. Given the growing interest in using TCIs as a metric for tracking aqueous alteration (e.g., Lentfort et al., 2021), Winchcombe is an exemplary sample for future studies exploring the mechanisms of TCI mineralization and the relationship between TCIs and the wider alteration environment.

Another distinctive property of the Winchcombe is the least-altered lithology (D). This is a rare example of a mildly altered CM chondrite. In recent years, several minimally altered CM chondrites have been identified. Winchcombe's lithology D is more altered than Paris (variously assigned CM2.7 or CM2.9; Hewins et al., 2014; Marrocchi et al., 2014; Rubin, 2015) and the Asuka CMs (A 12085 [CM2.8], A 12236 [CM2.9], and A 12169 [CM3.0]; Kimura et al., 2020). It represents a poorly sampled region of the CM alteration sequence, at the transition from early to intermediate alteration. We highlighted the unusual alteration of chondrule metal to goethite (instead of tochilinite) and suggested that lithology D may record early oxidizing microenvironments. The mineralogy, isotope chemistry, and alteration history of lithology D merits further detailed investigation and

comparison against Paris as both are recent CM falls with similar alteration extents.

We also studied Winchcombe's cataclastic matrix. It records the post-hydration history of the CM chondrites, specifically impact-induced fragmentation, and re-accretion. This component is found in all the brecciated CM chondrites, but it is rarely analyzed. Based on the fragmentation behavior of the Winchcombe meteoroid and the subsequent composition of the strewn field stones, we suggest that the strength of the cataclastic matrix is a critical factor in determining the survival of CM chondrite meteoroids. Future investigations should aim to quantify the strength of CM chondrite cataclastic matrix and determine the origin of the binding cement. Winchcombe's unweathered state makes this meteorite a priority sample for such an investigation.

CONCLUSIONS

At the millimeter scale, the Winchcombe meteorite is composed of lithic fragments. They sample the range of aqueous alteration extents (CM2.0–2.6) most commonly identified in CM chondrite meteorites (e.g., Rubin et al., 2007). Comparing mineral phases across lithologies allows the progression of aqueous alteration to be investigated. We focused on the generation and modification of TCIs. Our data suggest that large TCI clusters are formed by the pseudomorphic replacement of former multigrain carbonate aggregates. Regardless of the precursor phase (anhydrous silicate or carbonate), type II TCI formation followed a similar alteration sequence. Initially, inward dissolution by Fe-rich and S-rich fluids forms rims composed of intermixed tochilinite and cronstedtite. The intermediate stages of type II TCI formation are characterized by dissolution without concurrent precipitation forming hollow structures. These are later infilled most often by Mg-rich serpentine. As alteration advanced, early formed secondary phases became unstable and were either dissolved (e.g., T1a calcites) or chemically altered (e.g., TCI rims).

The use of TCIs in CM chondrites to evaluate the extent of aqueous alteration remains a useful and easily applied metric. However, an overreliance on this criterion at the expense of other criteria (e.g., extent of anhydrous silicate replacement, metal abundance, or carbonate generations) can lead to misidentification of alteration extent. This is because TCI compositions can vary significantly within a single CM chondrite lithology, and a calculated average masks local variability within the sample. We speculate that TCI compositional variability is due to two main factors: The effect of fluid-limited geochemical microenvironments that existed early in the alteration sequence, creating TCIs whose compositions reflect local rather than bulk fluid compositions, and because later reprocessing of TCIs during advanced aqueous alteration was incomplete, leaving relict compositions that reflect earlier epochs in the alteration sequence.

CM chondrite breccias are mixtures of lithic clasts held together by a weak cataclastic matrix. This material has not previously been studied in detail. In Winchcombe, the cataclastic matrix has a high porosity, abundant fractures, and is composed of subangular grains mostly with sizes <100 μm. It contains the full diversity of CM chondrite components (e.g., anhydrous silicates, carbonate grains, Fe-sulfides, TCIs, and blocks of fine-grained matrix). However, whole chondrules are rare (< 10 area%). The cataclastic matrix is interpreted as the fragmented and re-accreted debris produced by a high-energy impact into a CM chondrite parent body. The average grain size and the paucity of intact chondrules imply that fracturing (during disruption) cut through most large objects (transgranular fracture) while propagating around smaller objects (intergranular fracture).

Our study suggests that the weak cataclastic matrix influenced the fragmentation dynamics of the Winchcombe meteoroid, leading to its preferential separation into individual lithological clasts. Because most CM chondrites are also breccias, their survival is, likewise, dependent on the strength of their cataclastic matrix. A weak matrix will promote early disruption during atmospheric entry, reducing the chances of meteorite recovery. Winchcombe could, therefore, be a rare example of a poorly lithified CM chondrite. We predict an entire class of weak meteorites is missing from terrestrial collections.

Acknowledgments—This publication is part of the Winchcombe science team consortium, organized by the UK Fireball Alliance, and conducted by the UK Cosmochemistry Network. The authors of this paper would like to thank the UK Fireball Alliance, its constituent networks (UK Fireball Network, SCAMP, UKMON, AllSky7, NEMETODE, GMN), international collaborators (FRIPON, Global Fireball Observatory, Desert Fireball Network, University of Western Ontario, and University of Helsinki), and the meteor observation camera owners who participate in the UK Fireball Alliance network for their aid in observing the fireball and helping to predict its fall position. We would also like to thank the scientists and volunteers who participated in the UK Fireball Alliance–led search and recovery of the Winchcombe meteorite, and the local community, who generously reported and donated meteorite finds and enabled the team to search the strewn field. STFC are acknowledged for supporting the "Curation and Preliminary Examination of the Winchcombe Carbonaceous Chondrite Fall" project (ST/V000799/1),

and Natural History Museum staff for curatorial support. In addition, we acknowledge the following funding sources: AJK and HCB are funded by UK Research and Innovation (UKRI) grant MR/T020261/1. CSH is funded by STFC grant ST/V506904/1. LD thanks the University of Glasgow COVID-19-Research Support Scheme grant, and LD and MRL thank STFC grants (ST/T002328/1) and (ST/W001128/1) for support. The University of Kent thanks STFC for support via a consolidated grant in planetary science (ST/S000348/1). The University of Stirling thanks STFC for support via a training grant quota studentship (ST/V50709X/1). Work at the University of Manchester was supported by STFC grant ST/V000675/1. Finally, we thank Lionel Vacher and an anonymous reviewer and Associate Editor Yves Marrocchi for their helpful suggestions and comments, which greatly improved this work.

Conflicts of Interest—The authors declare that there are no conflicts of interest.

Data Availability Statement—The data that support the findings of this study are available in the supplementary material of this article.

Editorial Handling—Dr. Yves Marrocchi

REFERENCES

Alexander, C. M. O'D., Howard, K. T., Bowden, R., and Fogel, M. L. 2013. The Classification of CM and CR Chondrites Using Bulk H, C and N Abundances and Isotopic Compositions. *Geochimica et Cosmochimica Acta* 123: 244–60.

Alexander, C. M. O'D., Newsome, S. D., Fogel, M. L., Nittler, L. R., Busemann, H., and Cody, G. D. 2010. Deuterium Enrichments in Chondritic Macromolecular Material—Implications for the Origin and Evolution of Organics, Water and Asteroids. *Geochimica et Cosmochimica Acta* 74: 4417–37.

Andersen, J. C. Ø., Rollinson, G., Snook, B., Herrington, R., and Fairhurst, R. 2009. Use of QEMSCAN® for the Characterization of Ni-Rich and Ni-Poor Goethite in Laterite Ores. *Minerals Engineering* 22: 1119–29.

Baldwin, E. C., Milner, D. J., Burchell, M. J., and Crawford, I. A. 2007. Laboratory Impacts into Dry and Wet Sandstone with and Without an Overlying Water Layer: Implications for Scaling Laws and Projectile Survivability. *Meteoritics & Planetary Science* 42: 1905–14.

Bischoff, A., Ebert, S., Metzler, K., and Lentfort, S. 2017. Breccia Classification of CM Chondrites. *Meteoritics & Planetary Science* 52: A26.

Bischoff, A., Scott, E. R. D., Metzler, K., and Goodrich, C. A. 2006. Nature and Origins of Meteoritic Breccias. In *Meteorites and the Solar System II*, edited by D. S. Lauretta, and H. Y. McSween Jr, 679–712. Tucson, Arizona: The University of Arizona Press.

Brearley, A. J. 2006. The Action of Water. *Meteorites and the Early Solar System II* 943: 587–624.

Browning, L. B., McSween, H. Y., Jr., and Zolensky, M. E. 1996. Correlated Alteration Effects in CM Carbonaceous Chondrites. *Geochimica et Cosmochimica Acta* 60: 2621–33.

Buhl, E., Poelchau, M. H., Dresen, G., and Kenkmann, T. 2013. Deformation of Dry and Wet Sandstone Targets During Hypervelocity Impact Experiments, as Revealed from the MEMIN Program. *Meteoritics & Planetary Science* 48: 71–86.

Bunch, T. E., Chang, S., Frick, U., Neil, J., and Moreland, G. 1979. Carbonaceous Chondrites—I. Characterization and Significance of Carbonaceous Chondrite (CM) Xenoliths in the Jodzie Howardite. *Geochimica et Cosmochimica Acta* 43: 1727–42.

Cloutis, E. A., Hudon, P., Hiroi, T., Gaffey, M. J., and Mann, P. 2011. Spectral Reflectance Properties of Carbonaceous Chondrites: 2. CM Chondrites. *Icarus* 216: 309–46.

Cordier, C., and Folco, L. 2014. Oxygen Isotopes in Cosmic Spherules and the Composition of the Near Earth Interplanetary Dust Complex. *Geochimica et Cosmochimica Acta* 146: 18–26.

Cournede, C., Gattacceca, J., Gounelle, M., Rochette, P., Weiss, B. P., and Zanda, B. 2015. An Early Solar System Magnetic Field Recorded in CM Chondrites. *Earth and Planetary Science Letters* 410: 62–74.

Daly, L., Suttle, M. D., Lee, M. R., Bridges, J., Hicks, L., Martin, P.-E., Floyd, C. F., et al. 2022. Nano-Scale Heterogeneity in the Extent of Aqueous Alteration Within the Lithologies of the Winchcombe Meteorite. *Meteoritics & Planetary Science*.

Degawa, Y., Tomeoka, K., and Ikeda, Y. 1995. Precursors of PCP in CM Carbonaceous Chondrites. *Antarctic Meteorites* 20: 47–8.

Delbo, M., Walsh, K., Bolin, B., Avdellidou, C., and Morbidelli, A. 2017. Identification of a Primordial Asteroid Family Constrains the Original Planetesimal Population. *Science* 357: 1026–9.

Della Giustina, D. N., Emery, J. P., Golish, D. R., Rozitis, B., Bennett, C. A., Burke, K. N., Ballouz, R. L., et al. 2019. Properties of Rubble-Pile Asteroid (101955) Bennu from OSIRIS-REx Imaging and Thermal Analysis. *Nature Astronomy* 3: 341–51.

DeMeo, F. E., and Carry, B. 2013. The Taxonomic Distribution of Asteroids from Multi-Filter All-Sky Photometric Surveys. *Icarus* 226: 723–41.

Ebert, S., Patzek, M., Lentfort, S., and Bischoff, A. 2019. Accretion of Differentiated Achondritic and Aqueously Altered Chondritic Materials in the Early Solar System—Significance of an Igneous Fragment in the CM Chondrite NWA 12651. *Meteoritics & Planetary Science* 54: 2985–95.

Eiler, J. M., and Kitchen, N. 2004. Hydrogen Isotope Evidence for the Origin and Evolution of the Carbonaceous Chondrites. *Geochimica et Cosmochimica Acta* 68: 1395–411.

Elmaleh, A., Bourdelle, F., Caste, F., Benzerara, K., Leroux, H., and Devouard, B. 2015. Formation and Transformations of Fe-Rich Serpentines by Asteroidal Aqueous Alteration Processes: A Nanoscale Study of the Murray Chondrite. *Geochimica et Cosmochimica Acta* 158: 162–78.

Engrand, C., and Maurette, M. 1998. Carbonaceous Micrometeorites from Antarctica. *Meteoritics & Planetary Science* 33: 565–80.

Flynn, G. J., Durda, D. D., Sandel, L. E., Kreft, J. W., and Strait, M. M. 2009. Dust Production from the

Hypervelocity Impact Disruption of the Murchison Hydrous CM2 Meteorite: Implications for the Disruption of Hydrous Asteroids and the Production of Interplanetary Dust. *Planetary and Space Science* 57: 119–26.

Flynn, G. J., Durda, D. D., Sandel, L. E., and Strait, M. M. 2005. Dust Production from the Hypervelocity Impact Disruption of Hydrated Targets. *Earth, Moon, and Planets* 97: 213–31.

Fuchs, L. H., Olsen, E., and Jensen, K. J. 1973. Mineralogy, Mineral-Chemistry, and Composition of the Murchison (C2) Meteorite. *Smithsonian Contributions to the Earth Sciences* 10: 1–39. https://doi.org/10.5479/si.00810274.10.1.

Goodall, W. R., and Scales, P. J. 2007. An Overview of the Advantages and Disadvantages of the Determination of Gold Mineralogy by Automated Mineralogy. *Minerals Engineering* 20: 506–17.

Gottlieb, P., Wilkie, G., Sutherland, D., Ho-Tun, E., Suthers, S., Perera, K., Jenkins, B., Spencer, S., Butcher, A., and Rayner, J. 2000. Using Quantitative Electron Microscopy for Process Mineralogy Applications. *The Journal of The Minerals, Metals & Materials Society* 52: 24–5.

Grott, M., Biele, J., Michel, P., Sugita, S., Schröder, S., Sakatani, N., Neumann, W., Kameda, S., Michikami, T., and Honda, C. 2020. Macroporosity and Grain Density of Rubble Pile Asteroid (162173) Ryugu. *Journal of Geophysical Research: Planets* 125: 2020JE006519.

Hanna, R. D., Ketcham, R. A., Zolensky, M., and Behr, W. M. 2015. Impact-Induced Brittle Deformation, Porosity Loss, and Aqueous Alteration in the Murchison CM Chondrite. *Geochimica et Cosmochimica Acta* 171: 256–82.

Hanowski, N. P., and Brearley, A. J. 2000. Iron-Rich Aureoles in the CM Carbonaceous Chondrites Murray, Murchison, and Allan Hills 81002: Evidence for In Situ Aqueous Alteration. *Meteoritics & Planetary Science* 35: 1291–308.

Hanowski, N. P., and Brearley, A. J. 2001. Aqueous Alteration of Chondrules in the CM Carbonaceous Chondrite, Allan Hills 81002: Implications for Parent Body Alteration. *Geochimica et Cosmochimica Acta* 65: 495–518.

Hewins, R. H., Bourot-Denise, M., Zanda, B., Leroux, H., Barrat, J. A., Humayun, M., Göpel, C., et al. 2014. The Paris Meteorite, the Least Altered CM Chondrite So Far. *Geochimica et Cosmochimica Acta* 124: 190–222.

Hicks, L. J., Bridges, J. C., and Gurman, S. J. 2014. Ferric Saponite and Serpentine in the Nakhlite Martian Meteorites. *Geochimica et Cosmochimica Acta* 136: 194–210.

Howard, K. T., Benedix, G. K., Bland, P. A., and Cressey, G. 2009. Modal Mineralogy of CM2 Chondrites by X-Ray Diffraction (PSD-XRD). Part 1: Total Phyllosilicate Abundance and the Degree of Aqueous Alteration. *Geochimica et Cosmochimica Acta* 73: 4576–89.

Jenniskens, P., Fries, M. D., Yin, Q. Z., Zolensky, M., Krot, A. N., Sandford, S. A., Sears, D., et al. 2012. Radar-Enabled Recovery of the Sutter's Mill Meteorite, a Carbonaceous Chondrite Regolith Breccia. *Science* 338: 1583–7.

Jilly-Rehak, C. E., Huss, G. R., Nagashima, K., and Schrader, D. L. 2018. Low-Temperature Aqueous Alteration on the CR Chondrite Parent Body: Implications from In Situ Oxygen-Isotope Analyses. *Geochimica et Cosmochimica Acta* 222: 230–52.

Kerraouch, I., Ebert, S., Patzek, M., Bischoff, A., Zolensky, M. E., Pack, A., Schmitt-Kopplin, P., Belhai, D., Bendaoud, A., and Le, L. 2019. A Light, Chondritic Xenolith in the Murchison (CM) Chondrite–Formation by Fluid-Assisted Percolation During Metasomatism? *Geochemistry* 79: 125518.

Kimura, M., Imae, N., Komatsu, M., Barrat, J. A., Greenwood, R. C., Yamaguchi, A., and Noguchi, T. 2020. The Most Primitive CM Chondrites, Asuka 12085, 12169, and 12236, of Subtypes 3.0–2.8: Their Characteristic Features and Classification. *Polar Science* 26: 100565.

King, A. J., Daly, L., Rowe, J., Joy, K. H., Greenwood, R. C., Devillepoix, H. A., Suttle, M. D., et al. 2022. The Winchcombe Meteorite, a Unique and Pristine Witness from the Outer Solar System. *Science Advances* 8: eabq3925.

King, A. J., Russell, S. S., Schofield, P. F., Humphreys-Williams, E. R., Strekopytov, S., Abernethy, F. A. J., Verchovsky, A. B., and Grady, M. M. 2019. The Alteration History of the Jbilet Winselwan CM Carbonaceous Chondrite: An Analog for C-Type Asteroid Sample Return. *Meteoritics & Planetary Science* 54: 521–43.

Krietsch, D., Busemann, H., Riebe, M. E., King, A. J., Alexander, C. M. O'D., and Maden, C. 2021. Noble Gases in CM Carbonaceous Chondrites: Effect of Parent Body Aqueous and Thermal Alteration and Cosmic Ray Exposure Ages. *Geochimica et Cosmochimica Acta* 310: 240–80.

Krzesińska, A., and Fritz, J. 2014. Weakly Shocked and Deformed CM Microxenoliths in the Puøtusk H Chondrite. *Meteoritics & Planetary Science* 49: 595–610.

Kurat, G., Koeberl, C., Presper, T., Brandstätter, F., and Maurette, M. 1994. Petrology and Geochemistry of Antarctic Micrometeorites. *Geochimica et Cosmochimica Acta* 58: 3879–904.

Lauretta, D. S., DellaGiustina, D. N., Bennett, C. A., Golish, D. R., Becker, K. J., Balram-Knutson, S. S., Barnouin, O. S., et al. 2019. The Unexpected Surface of Asteroid (101955) Bennu. *Nature* 568: 55–60.

Le Guillou, C., Changela, H. G., and Brearley, A. J. 2015. Widespread Oxidized and Hydrated Amorphous Silicates in CR Chondrites Matrices: Implications for Alteration Conditions and H2 Degassing of Asteroids. *Earth and Planetary Science Letters* 420: 162–73.

Lee, M. R., Cohen, B. E., King, A. J., and Greenwood, R. C. 2019. The Diversity of CM Carbonaceous Chondrite Parent Bodies Explored Using Lewis Cliff 85311. *Geochimica et Cosmochimica Acta* 264: 224–44.

Lee, M. R., and Greenwood, R. C. 1994. Alteration of Calcium- and Aluminium-Rich Inclusions in the Murray (CM2) Carbonaceous Chondrite. *Meteoritics* 29: 780–90.

Lee, M. R., Lindgren, P., and Sofe, M. R. 2014. Aragonite, Breunnerite, Calcite and Dolomite in the CM Carbonaceous Chondrites: High Fidelity Recorders of Progressive Parent Body Aqueous Alteration. *Geochimica et Cosmochimica Acta* 144: 126–56.

Lee, M. R., Sofe, M. R., Lindgren, P., Starkey, N. A., and Franchi, I. A. 2013. The Oxygen Isotope Evolution of Parent Body Aqueous Solutions as Recorded by Multiple Carbonate Generations in the Lonewolf Nunataks 94101 CM2 Carbonaceous Chondrite. *Geochimica et Cosmochimica Acta* 121: 452–66.

Lentfort, S., Bischoff, A., Ebert, S., and Patzek, M. 2021. Classification of CM Chondrite Breccias—Implications for

the Evaluation of Samples from the OSIRIS-REx and Hayabusa 2 Missions. *Meteoritics & Planetary Science* 56: 127–47.

Leroux, H., Cuvillier, P., Zanda, B., and Hewins, R. H. 2015. GEMS-Like Material in the Matrix of the Paris Meteorite and the Early Stages of Alteration of CM Chondrites. *Geochimica et Cosmochimica Acta* 170: 247–65.

Lindgren, P., Hanna, R. D., Dobson, K. J., Tomkinson, T., and Lee, M. R. 2015. The Paradox Between Low Shock-Stage and Evidence for Compaction in CM Carbonaceous Chondrites Explained by Multiple Low-Intensity Impacts. *Geochimica et Cosmochimica Acta* 148: 159–78.

Mackinnon, I. D. R., and Zolensky, M. E. 1984. Proposed Structures for Poorly Characterized Phases in C2M Carbonaceous Chondrite Meteorites. *Nature* 309: 240–2.

Marrocchi, Y., Delbo, M., and Gounelle, M. 2021. The Astrophysical Context of Collision Processes in Meteorites. *Meteoritics & Planetary Science* 56: 1406–21. https://doi.org/10.1111/maps.13716.

Marrocchi, Y., Gounelle, M., Blanchard, I., Caste, F., and Kearsley, A. T. 2014. The Paris CM Chondrite: Secondary Minerals and Asteroidal Processing. *Meteoritics & Planetary Science* 49: 1232–49.

McMullan, S., Vida, D., Devillepoix, H. A. R., Rowe, J., Daly, L., King, A. J., Cupák, M., et al. 2022. The Winchcombe Fireball—that Lucky Survivor. *Meteoritics & Planetary Science*.

McSween, H. Y., Jr. 1979. Alteration in CM Carbonaceous Chondrites Inferred from Modal and Chemical Variations in Matrix. *Geochimica et Cosmochimica Acta* 43: 1761–70.

Metzler, K., Bischoff, A., and Stöffler, D. 1992. Accretionary Dust Mantles in CM Chondrites: Evidence for Solar Nebula Processes. *Geochimica et Cosmochimica Acta* 56: 2873–97.

Musolino, A. 2021. Exploring the Variability of Primitive Materials and Processes in the Early Solar System: Characterisation of Four Chondritic Meteorites. Published Masters' thesis, University of Pisa. https://etd.adm.unipi.it/t/etd-05162021-112610/.

Nakamura, T. 2006. Yamato 793321 CM Chondrite: Dehydrated Regolith Material of a Hydrous Asteroid. *Earth and Planetary Science Letters* 242: 26–38.

Nakamura, T., Nagao, K., Metzler, K., and Takaoka, N. 1999. Heterogeneous Distribution of Solar and Cosmogenic Noble Gases in CM Chondrites and Implications for the Formation of CM Parent Bodies. *Geochimica et Cosmochimica Acta* 63: 257–73.

Nakamura, T., and Nakamuta, Y. 1996. X-Ray Study of PCP from the Murchison CM Carbonaceous Chondrite. *Antarctic Meteorite Research* 9: 37–50.

Palmer, E. E., and Lauretta, D. S. 2011. Aqueous Alteration of Kamacite in CM Chondrites. *Meteoritics & Planetary Science* 46: 1587–607.

Patzek, M., Bischoff, A., Visser, R., and John, T. 2018. Mineralogy of Volatile-Rich Clasts in Brecciated Meteorites. *Meteoritics & Planetary Science* 53: 2519–40.

Patzek, M., Hoppe, P., Bischoff, A., Visser, R., and John, T. 2020. Hydrogen Isotopic Composition of CI- and CM-Like Clasts from Meteorite Breccias—Sampling Unknown Sources of Carbonaceous Chondrite Materials. *Geochimica et Cosmochimica Acta* 272: 177–97.

Peng, Y., and Jing, Y. 2014. Hydrothermal Preparation of Analogous Matrix Minerals of CM Carbonaceous Chondrites from Metal Alloy Particles. *Earth and Planetary Science Letters* 408: 252–62.

Pignatelli, I., Marrocchi, Y., Mugnaioli, E., Bourdelle, F., and Gounelle, M. 2017. Mineralogical, Crystallographic and Redox Features of the Earliest Stages of Fluid Alteration in CM Chondrites. *Geochimica et Cosmochimica Acta* 209: 106–22.

Pignatelli, I., Marrocchi, Y., Vacher, L. G., Delon, R., and Gounelle, M. 2016. Multiple Precursors of Secondary Mineralogical Assemblages in CM Chondrites. *Meteoritics & Planetary Science* 51: 785–805.

Pirrie, D., and Rollinson, G. K. 2011. Unlocking the Applications of Automated Mineral Analysis. *Geology Today* 27: 235–44.

Rollinson, G. K., Stickland, R. J., Andersen, J. C., Fairhurst, R., and Boni, M. 2011. Characterisation of Supergene Non-Sulphide Zinc Deposits Using QEMSCAN®. *Minerals Engineering* 24: 778–87.

Rosenberg, N. D., Browning, L., and Bourcier, W. L. 2001. Modeling Aqueous Alteration of CM Carbonaceous Chondrites. *Meteoritics & Planetary Science* 36: 239–44.

Rubin, A. E. 2015. An American on Paris: Extent of Aqueous Alteration of a CM Chondrite and the Petrography of its Refractory and Amoeboid Olivine Inclusions. *Meteoritics & Planetary Science* 50: 1595–612.

Rubin, A. E., Trigo-Rodríguez, J. M., Huber, H., and Wasson, J. T. 2007. Progressive Aqueous Alteration of CM Carbonaceous Chondrites. *Geochimica et Cosmochimica Acta* 71: 2361–82.

Schindelin, J., Arganda-Carreras, I., Frise, E., Kaynig, V., Longair, M., Pietzsch, T., Preibisch, S., et al. 2012. Fiji: An Open-Source Platform for Biological-Image Analysis. *Nature Methods* 9: 676–82.

Schröckenfuchs, T., Bauer, H., Grasemann, B., and Decker, K. 2015. Rock Pulverization and Localization of a Strike-Slip Fault Zone in Dolomite Rocks. *Journal of Structural Geology* 78: 67–85.

Stephen, N. R., Benedix, G. K., Bland, P., Howard, K. T. & Hamilton, V. E. 2010. Modal Mineralogy of the Martian Meteorite Zagami (Abstract #1533). 41st Lunar and Planetary Science Conference. CD-ROM.

Suttle, M. D., Genge, M. J., Folco, L., and Russell, S. S. 2017. The Thermal Decomposition of Fine-Grained Micrometeorites, Observations from Mid-IR Spectroscopy. *Geochimica et Cosmochimica Acta* 206: 112–36.

Suttle, M. D., King, A. J., Ramkissoon, N. K., Bonato, E., Franchi, I. A., Malley, J., Schofield, P. F., Najorka, J., Salge, T., and Russell, S. S. 2022. Alteration Conditions on the CM and CV Parent Bodies—Insights from Hydrothermal Experiments with the CO Chondrite Kainsaz. *Geochimica et Cosmochimica Acta* 318: 83–111.

Suttle, M. D., King, A. J., Schofield, P. F., Bates, H., and Russell, S. S. 2021. The Aqueous Alteration of CM Chondrites, a Review. *Geochimica et Cosmochimica Acta* 299: 219–56.

Taylor, S., Matrajt, G., and Guan, Y. 2012. Fine-Grained Precursors Dominate the Micrometeorite Flux. *Meteoritics & Planetary Science* 47: 550–64.

The Meteoritical Bulletin. 2022. https://www.lpi.usra.edu/meteor/. Accessed August 5, 2022.

Tomeoka, K., and Buseck, P. R. 1985. Indicators of Aqueous Alteration in CM Carbonaceous Chondrites: Microtextures of a Layered Mineral Containing Fe, S, O and Ni. *Geochimica et Cosmochimica Acta* 49: 2149–63.

Tomeoka, K., Kiriyama, K., Nakamura, K., Yamahana, Y., and Sekine, T. 2003. Interplanetary Dust from the Explosive Dispersal of Hydrated Asteroids by Impacts. *Nature* 423: 60–2.

Vacher, L. G., Marrocchi, Y., Villeneuve, J., Verdier-Paoletti, M. J., and Gounelle, M. 2017. Petrographic and C & O Isotopic Characteristics of the Earliest Stages of Aqueous Alteration of CM Chondrites. *Geochimica et Cosmochimica Acta* 213: 271–90.

Vacher, L. G., Marrocchi, Y., Villeneuve, J., Verdier-Paoletti, M. J., and Gounelle, M. 2018. Collisional and Alteration History of the CM Parent Body. *Geochimica et Cosmochimica Acta* 239: 213–34.

Vacher, L. G., Truche, L., Faure, F., Tissandier, L., Mosser-Ruck, R., and Marrocchi, Y. 2019. Deciphering the Conditions of Tochilinite and Cronstedtite Formation in CM Chondrites from Low Temperature Hydrothermal Experiments. *Meteoritics & Planetary Science* 54: 1870–89.

Van Kooten, E. M., Cavalcante, L. L., Nagashima, K., Kasama, T., Balogh, Z. I., Peeters, Z., Hsiao, S. S. Y., et al. 2018. Isotope Record of Mineralogical Changes in a Spectrum of Aqueously Altered CM Chondrites. *Geochimica et Cosmochimica Acta* 237: 79–102.

Velbel, M. A., Tonui, E. K., and Zolensky, M. E. 2012. Replacement of Olivine by Serpentine in the Carbonaceous Chondrite Nogoya (CM2). *Geochimica et Cosmochimica Acta* 87: 117–35.

Velbel, M. A., Tonui, E. K., and Zolensky, M. E. 2015. Replacement of Olivine by Serpentine in the Queen Alexandra Range 93005 Carbonaceous Chondrite (CM2): Reactant–Product Compositional Relations, and Isovolumetric Constraints on Reaction Stoichiometry and Elemental Mobility During Aqueous Alteration. *Geochimica et Cosmochimica Acta* 148: 402–25.

Verdier-Paoletti, M. J., Marrocchi, Y., Vacher, L. G., Gattacceca, J., Gurenko, A., Sonzogni, C., and Gounelle, M. 2019. Testing the Genetic Relationship Between Fluid Alteration and Brecciation in CM Chondrites. *Meteoritics & Planetary Science* 54: 1692–709.

Vernazza, P., Marsset, M., Beck, P., Binzel, R. P., Birlan, M., Cloutis, E. A., DeMeo, F. E., Dumas, C., and Hiroi, T. 2016. Compositional Homogeneity of CM Parent Bodies. *The Astronomical Journal* 152: 54.

Walsh, K. J. 2018. Rubble Pile Asteroids. *Annual Review of Astronomy and Astrophysics* 56: 593–624.

Wasson, J. T., Boynton, W. V., Chou, C. L., and Baedecker, P. A. 1975. Compositional Evidence Regarding the Influx of Interplanetary Materials onto the Lunar Surface. *The Moon* 13: 121–41.

Wilson, L., Keil, K., Browning, L. B., Krot, A. N., and Bourcier, W. 1999. Early Aqueous Alteration, Explosive Disruption, and Reprocessing of Asteroids. *Meteoritics & Planetary Science* 34: 541–57.

Yugami, K., Takeda, H., Kojima, H., and Miyamoto, M. 1998. Modal Mineral Abundances and the Differentiation Trends in Primitive Achondrites. Antarctic Meteorite Research. 22nd Symposium on Antarctic Meteorites, NIPR Symposium No. 11.

Zolensky, M., Barrett, R., and Browning, L. 1993. Mineralogy and Composition of Matrix and Chondrule Rims in Carbonaceous Chondrites. *Geochimica et Cosmochimica Acta* 57: 3123–48.

Zolensky, M. E. 1984. Hydrothermal Alteration of CM Carbonaceous Chondrites: Implications of the Identification of Tochilinite as One Type of Meteoritic PCP. 47th Annual Meeting of the Meteoritical Society 537: 19.

Zolensky, M. E., Mittlefehldt, D. W., Lipschutz, M. E., Wang, M. S., Clayton, R. N., Mayeda, T. K., Grady, M. M., Pillinger, C., and David, B. 1997. CM Chondrites Exhibit the Complete Petrologic Range from Type 2 to 1. *Geochimica et Cosmochimica Acta* 61: 5099–115.

SUPPORTING INFORMATION

Additional supporting information may be found in the online version of this article.

Appendix S1. Additional supporting data. This includes detailed petrographic descriptions for all Winchcombe lithologies, chemical data, structual data and SEM images of all sections studied.